Modeling of Radiative Processes in Organic Scintillators

Jenny Nilsson

Department of Radiation Physics
Department of Physics
Faculty of Science
University of Gothenburg

UNIVERSITY OF GOTHENBURG

Gothenburg 2014-02-17

☹ 😐 ☺

Modeling of Radiative Processes in Organic Scintillators

Jenny Nilsson

Department of Radiation Physics
Department of Physics
Faculty of Science
University of Gothenburg

ABSTRACT

This thesis presents the development of a Monte Carlo calibration of a whole body counter (WBC), consisting of four large plastic (organic) scintillators, used for determine the body burden of gamma-emitting radionuclides. A scintillator emits optical photons after energy has been deposited by an ionizing particle in the scintillator material. The optical photons are converted into an electric signal by two photomultiplier tubes (PMT) mounted on each plastic scintillator and the final output from the WBC is an energy spectrum. The Monte Carlo model should accurately predict a measured energy spectrum, which requires a detailed model of the radiative processes in the scintillators. In Paper I the geometrical Monte Carlo model of the WBC is verified by comparing the simulated total efficiency (using MCNPX) with the measured total efficiency. Paper I shows that optical physics needed to be included in the Monte Carlo model. Paper II shows that the Monte Carlo code GATE, which can transport ionizing particles and optical photons, can be used to model the plastic scintillators. Paper II also presents a method to model the PMT response in MATLAB. Paper III presents a thorough study of the optical transport in GATE and identifies the key parameters for describing the optical physics processes at a scintillator surface. The Monte Carlo model is verified in Paper IV by comparing simulated results with measured result. Paper IV also presents the final step in the Monte Carlo calibration process by implementing the ICRP human computational phantoms into the Monte Carlo model of the WBC.

SAMMANFATTNING PÅ SVENSKA

Efter till exempel olyckor eller andra händelser med radioaktiva ämnen så finns det en risk att människor får i sig radioaktiva ämnen, radionuklider, genom exempelvis inandning eller intag av kontaminerad föda. Det är viktigt att kunna fastställa om en individ har fått i sig en radionuklid och i så fall hur mycket, men precis lika viktigt är att kunna ge beskedet att inget intag har skett. Helkroppsmätningar är en metod som ofta används för att bestämma kroppsinnehållet av radionuklider som sänder ut gammastrålning. Vid en helkroppsmätning placeras detektorer nära kroppen. En detektor registrerar ett visst antal gammafotoner beroende på hur mycket av en radionuklid som finns i kroppen och om sambandet är känt kan kroppsinnehållet av radionukliden bestämmas. Sambandet ser olika ut beroende på bland annat vilken typ av radionuklid det är samt hur den är fördelad i kroppen.

Hur en gammafoton växelverkar i en detektor kan beskrivas statistiskt då sannolikheten för olika växelverkansprocesser är kända. Detta gör det möjligt att göra en datorsimulering av hur en detektor för helkroppsmätning registrerar en specifik radionuklid med avseende på dess fördelning i kroppen. Datormodeller som bygger på statistiska processer där utfallet beror på olika sannolikheter brukar benämnas Monte Carlo-simuleringar. I detta arbete har Monte Carlo-simuleringar gjorts för detektorer som består av ett plastmaterial som sänder ut optiska fotoner (ljus) då gammafotoner växelverkar i plasten. De optiska fotonerna detekteras och omvandlas till en elektrisk signal. Signalens utseende beror på andelen optiska fotoner och en analys av signalen ger information om gammafotonen, vilken i sin tur ger information om radionukliden. Även de optiska fotonernas växelverkan i detektorn inkluderades i Monte Carlo-simuleringarna.

För att koppla detektorresponsen till mätningar på en människa infogades en detaljerad digital 3D-representation av både en man och en kvinna, baserad på medicinska datortomografiska bilder (skiktröntgen), i datormodellen. Detta gör det möjligt att simulera detektorresponsen för en valfri radionuklid i en valfri vävnad. Detektorn kan sedan användas vid helkroppsmätningar för att kvantifiera ett okänt kroppsinnehåll av samma radionuklid som i simuleringarna.

LIST OF PAPERS

This thesis is based on the following papers, referred to in the text by their Roman numerals.

I.   Nilsson J and Isaksson M 2010 A comparison between Monte Carlo calculated and measured total efficiencies and energy resolution for large plastic scintillators used in whole body counting *Radiation Protection Dosimetry* **144** 555-559

II.   Nilsson J and Isaksson M 2013 The design of a low activity laboratory housing a whole body counter consisting of large plastic scintillators and the work towards a flexible Monte Carlo calibration *Accepted for publication in Progress in Nuclear Science and Technology*

III.   Nilsson J, Cuplov V and Isaksson M 2014 Identifying the key parameters for optical photon transport simulations using GEANT4/GATE *Submitted to Physics in Medicine and Biology*

IV.   Nilsson J and Isaksson M 2014 A Monte Carlo calibration of a whole body counter using the ICRP computational phantoms *Submitted to Radiation Protection Dosimetry*

Preliminary results have been presented as follows

A comparison between Monte Carlo simulated and measured total efficiencies and energy resolution, for large plastic scintillators used in whole body counting
Nilsson J and Isaksson M
Poster presentation at the European Conference on Individual Monitoring of Ionizing Radiation March 8 – 12, 2010, Athens Greece

Whole body counting with large plastic scintillators as a tool in emergency preparedness – determination of total efficiency and energy resolution
Nilsson J and Isaksson M
Poster presentation at the Third European IRPA Congress 2010 June 14 – 18, Helsinki, Finland

Towards a flexible calibration of a whole body counter
Nilsson J and Isaksson M
Poster presentation at the European Radiation Research meeting 5 – 9 September 2010, Stockholm, Sweden

Monte Carlo calibration of large plastic scintillators using MCNPX 2.6.0: highlighting the need of increased model complexity when simulating measured pulse height spectra with pulse height energy deposition spectra
Nilsson J and Isaksson M
Poster presentation at MC2010 Stockholm, 9 – 12 November 2010, Stockholm, Sweden

Towards a flexible Monte Carlo calibration of a whole body counter spectrometer system – Highlighting the need of increased model complexity for large plastic scintillators
Nilsson J
Licentiate seminar, University of Gothenburg, 11 may 2011, Göteborg, Sweden

The design of a low activity laboratory housing a whole body counter consisting of large plastic scintillators and the work towards a flexible Monte Carlo calibration
Nilsson J and Isaksson M
Poster presentation at 12th International Conference on Radiation Shielding, 2 – 4 September 2012, Nara, Japan

Can gate be used for Monte Carlo calibrations of whole body counters?
Nilsson J and Isaksson M
Poster presentation at 13th International IRPA Congress, 13 – 18 May 2013, Glasgow, Scotland

The impact of surface properties on optical transport in plastic scintillation detectors
Nilsson J and Isaksson M
Oral presentation at GEANT4 2013 International user conference, 7 – 9 October 2013, Bordeaux, France

CONTENTS

1 INTRODUCTION

In the early 60's a bunker was built to temporary house a ^{60}Co radiation therapy unit at the Sahlgrenska University Hospital, Sweden. It was decided from the beginning that the bunker would be used as a low activity laboratory after the unit had been moved and the design and building material was chosen to suit both purposes [1]. Today, the laboratory has two whole body counters (WBC), system I and system II, housed in a twin steel chamber. The WBC systems are capable of quantifying low concentrations of radioactive body burdens, emitting gamma photons, and have been used for metabolic studies, radiation protection measurements and total body potassium content measurements [2-15].

In the beginning of the 21 century The Swedish Radiation Safety Authority and the Swedish Civil Contingencies Agency recognized that the emergency preparedness for emergencies involving radioactive materials was declining. One measure to restore and reinforce the preparedness organization was to make an inventory of available measurement systems and invest in new equipment to adapt the system to emergency preparedness demands. The low activity laboratory at Sahlgrenska has the capacity to detect and quantify low activities of radionuclides accumulated in the human body and it could be used for contamination measurements given that at least one of the WBC is calibrated with respect to the nuclide, source distribution and body type. A WBC is normally calibrated for a known geometry and radionuclide but in an emergency there is a short time interval between the knowledge of what to measure and when it needs to be measured. A calibration method well suited for this kind of situations is the Monte Carlo calibration, in which a detector response is simulated using the Monte Carlo method. By including a human computational phantom in the Monte Carlo simulations, the WBC can be calibrated for an optional radionuclide and its distribution in an optical tissue within a short notice. This motivated the Swedish Radiation Safety Authority and the Swedish Civil Contingencies Agency to fund a PhD project aimed to develop a Monte Carlo calibration of a WBC, and the result of the project is presented this thesis.

1.1   A short presentation of the aim and the four papers

System I consists of two NaI(Tl) detector in a scanning bed geometry and system II of four large plastic scintillators (each measuring 91.5 × 76.0 × 25.4 cm^3). The papers presented in this thesis have been made using system II only. A schematic of system II is shown in Figure 9, section 3.1.

The production of a signal from a scintillator in system II can be divided into five major steps [16]:

1)   An ionizing particle deposits energy in the scintillator and electrons are excited. The number of excited electrons corresponds to the initial energy deposition. The following relaxation of the excited states results in an emission of optical (scintillation) photons.

2)   The optical photons travel through the scintillator and lightguide and undergo photoelectric absorption the photocathode of a photomultiplier tube (PMT).

3)   Photoelectrons leave the photocathode.

4)   The photoelectrons are collected at the first dynode in the PMT.

5)   Multiplication in the PMT.

Step 6 explains the final output from the WBC

6)   Two PMT are mounted on the short end of each scintillator, the output from the PMT are summed detector-wise, amplified and fed into a multichannel analyzer (MCA) that produces an energy spectrum. The energy spectrum can be shown detector-wise or as the sum of the energy spectra from two, three or four detectors.

In an ideal spectrometer system the energy spectrum from the MCA corresponds directly to the energy deposited by an ionizing particle (step 1). However, an energy deposition spectrum differs quite drastically from a measured energy spectrum. Figure 1 shows the difference in obtained energy spectrum from system II, using the Monte Carlo method (left) and through measurements (right), for a ^{137}Cs point source at three source positions, see Figure 9b for source positions. The Monte Carlo simulation only included step 1 whereas the measured energy spectrum includes steps 1 – 6. Due to the processes occurring after energy deposition the measured energy spectrum shows a drastic decrease in energy resolution (the de-

crease in energy resolution is not specific for plastic scintillators and can be seen in the energy spectrum from all scintillators). The measured energy spectrum shifts as the source is moved away from the PMT, from 70 cm to 30 cm.
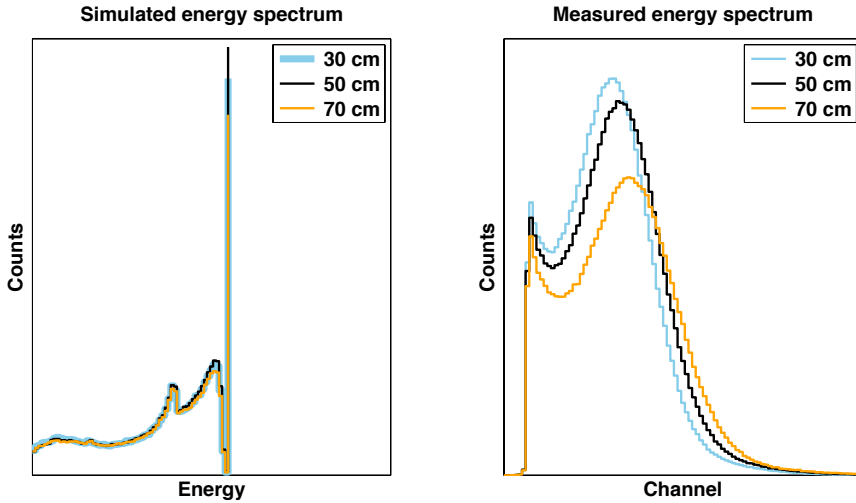
Figure 1. The energy spectrum obtained for a ^{137}Cs point source at three source positions obtained using detector 1 in Figure 9. To the left is the Monte Carlo simulated energy deposition spectrum and to the right the measured energy spectrum.

The aim of the thesis is to make a Monte Carlo calibration of the WBC in system II. This was done by making a Monte Carlo model of the WBC, where steps 1 - 6 were included in the model. The simulated WBC response was compared to the measured response for three gamma-emitting radionuclides. Thereafter, a human computational phantom was included in the Monte Carlo model and the WBC response was simulated for two heterogeneously distributed radionuclides. The distribution of the radionuclides in the phantoms was based on biokinetic models.

1.1.1 Paper I

Paper I [17] presented a verification of the geometrical model of the WBC, argued for an energy spectrum broadening function based on the physics processes in steps 1 – 5 presented in section 1.1 and investigated the impact of a nonlinear light yield on the simulated energy deposition

spectrum. The Monte Carlo code used was MCNPX 2.6.0 (Monte Carlo N Particle eXtended) [18], which is a general-purpose code capable of transporting neutrons, photons, electrons, protons and heavy ions over a broad range of energies. The code is developed and maintained by LANL, Los Alamos National Laboratory, USA.

In a Monte Carlo simulation a source particle is transported through matter and in each interaction more particles can be created. All particles are followed until they are either absorbed or killed. The generated data for all particles created during the run of one source particle are scored from a volume(s) defined by the user. The scored data is referred to as a particle history throughout this thesis.

In Paper I the energy deposition in the plastic scintillator per particle history was simulated. The simulated energy spectrum could not be compared to the measured energy spectrum due to the large differences in energy resolution, see Figure 1, and the verification of the geometrical model was made by comparing the simulated total efficiency (using the sum of all scored gamma photons in an energy spectrum) with the measured total efficiency for a ^{137}Cs point source. In the measured energy spectrum lower channels had to be discriminated due to noise and an equivalent discrimination must then be applied in the simulated energy deposition spectrum as well, i.e. scored particles below a certain energy should be discriminated. However, the discrimination level was unknown since a plastic scintillator cannot be energy calibrated due to its poor energy resolution. Paper I presented an approach, using the Monte Carlo simulations, to determine the energy of the discrimination level in the measured energy spectrum.

A simulated energy deposition spectrum in MCNPX can be broadened using the function GEB (Gaussian Energy Broadening [18]). A Gaussian broadening function can be used when simulating the energy spectrum from plastic scintillators [19, 20], as well as inorganic scintillators [21] or semi-conductive detectors [22]. However, Paper I showed that it would not be a suitable method for simulating the energy spectrum from a large plastic scintillator. Instead Paper I argued for suing the broadening function first proposed by Breitenberger [16], which considers the impact of steps $1 - 5$ in section 1.1

Ideally the emitted light from a scintillator is linear to the energy deposition. This is true for fast electrons but for heavy particles or electrons be-

low 125 keV the relationship is nonlinear [23]. Paper I studied if a nonlinear light yield would have an impact on the simulated energy deposition spectrum obtained for a plastic scintillator. MCNPX 2.6.0 does not support generation of optical photons nor optical photon transport but it has the capability to simulate emitted light, L, per particle history where L is expressed in MeVee (MeV electron equivalent). 1 MeVee is defined as the emitted light from a scintillator after a fast electron of 1 MeV deposits its entire energy in a scintillating material. MCNPX calculates L by multiplying $\partial L/\partial E$ (emitted fluorescent light per deposited energy) with the total energy, E, deposited by an electron. A simulated spectrum of emitted light, unit MeVee, is equivalent to a simulated energy deposition spectrum, unit MeV, if the light yield is linear for all energies. The MCNPX user needs to define $\partial L/\partial E$, which can be calculated using Birks' formula (see section 2.1.3) if Birks's constant, kB, is known. Birks' constant is scintillator specific and Paper I presented a method to determine Birks' constant for the plastic scintillators used in the WBC in system II. The impact of a nonlinear light yield was studied by comparing a simulated emitted light spectrum for a linear light yield with a simulated emitted light spectrum for a nonlinear light yield.

1.1.2   Interlude

This study [24] is not a part of the thesis but the knowledge gained from it was important for the direction taken in Paper II – IV. In this work MCNPX 2.6.0 was used to study the impact of bulk absorption, absorption of an optical photon by the scintillator material, which results in a signal loss. The probability for bulk absorption increases with distance travelled in the scintillator by an optical photon. This was modeled as a decrease of emitted light per deposited energy, $\partial L/\partial E$, as the distance between the PMT and energy deposition site increased. It was not an attempt to correctly describe bulk absorption but a simple test to study if bulk absorption had an impact on an energy spectrum. Two simulations were performed with a [54]Mn source (modeled as a mono-energetic gamma-emitter with energy 834.848 keV) placed at two distances from the PMT. For each position the spectrum of emitted light was scored. The results are shown in Figure 2, where the green spectrum is for the source position closest to the PMT.
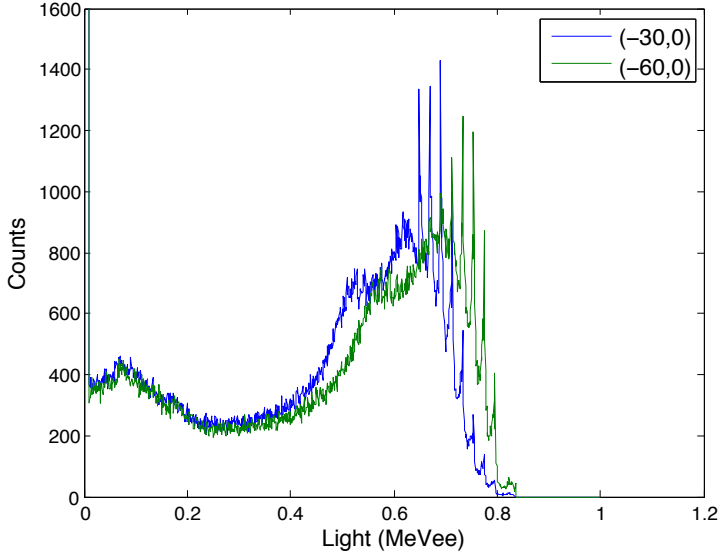
Figure 2. Two simulated light emittance spectrum for a [54]Mn point source placed at two different positions: (-30, 0) and (-60,0), where source position (-60,0) is closest to the PMT. Source position (-30,0) is the same as source position 30 cm in Figure 9b. Figure 2 has been published in the IRPA 2013 conference proceedings [a].

Figure 2 shows that the simulated spectrum of emitted light starts to resemble the measured energy spectrum seen in Figure 1; the energy resolution decreases and the spectrum shifts as the source is moved away from the PMT. Based on the results presented in Figure 2 it was concluded that the transport of optical photons needed to be included into the Monte Carlo model of system II.

1.1.3   Paper II

Paper II [25] studied if the Monte Carlo code GATE (GEANT4 Application for Tomographic Emission) [26-28] could be used to model the WBC in system II. GATE is an advanced open-source software dedicated to Monte Carlo simulations of preclinical and clinical scans in emission tomography, transmission tomography and radiation therapy. GATE is a scripted macro language that uses the GEANT4 [29] libraries for all simulations and GEANT4 is a simulation toolkit capable of transporting optical

photons as well as ionizing particles through matter. GEANT4 is a general-purpose code and everything that can be simulated in GATE can be simulated in GEANT4, but everything that can be simulated in GEANT4 cannot be simulated in GATE. GEANT4 is written in C++ and, unless the user is very familiar with C++, is a quite complicated Monte Carlo code. In that aspect GATE is more user-friendly since it requires very little, if any, knowledge of C++.

WBC systems and imaging systems based on emission tomography, SPECT and PET, are based on the same basic principles: an ionizing particle deposits energy in a scintillator; optical photons are emitted, detected and converted into an electric signal. The aim of Paper II was to study if GATE could be used for modeling a WBC system where the optical transport in the scintillators were included. If so, the small field of emergency preparedness and whole body counting could take advantage of the Monte Carlo code development made in the much larger field of medical imaging.

The geometrical Monte Carlo model of the WBC was, with a few minor exceptions, identical to the model presented in Paper I (this is further explain in the section 3.1). The Monte Carlo model in Paper II also included the generation of optical photons and their transport through the scintillator, the detection of optical photons by a photocathode and the multiplication in the PMTs (steps 1 – 5 in section 1.1). The PMT response was coupled to the optical transport and calculated in MATLAB [30].

For optical transport simulations in GEANT4/GATE, the user needs to define material parameters and surface parameters. The material parameters control the scintillation and the transport of optical photons through a material and the surface parameters control the physics processes (reflection, refraction, absorption) an optical photon undergoes when reaching a boundary between two volumes. Most of the material parameters can be obtained from the manufacturer of the scintillator but the surface parameters are specific for a certain system. The surface parameters for the WBC system is unknown and a literature search was made to find possible parameter values.

Three types of spectra were simulated in Paper II: the energy deposition spectrum (same as in Paper I), the optical spectrum and the PMT spectrum. The optical spectrum is the number of detected optical photons by the photocathode per particle history and the PMT spectrum the number

of generated electrons by the PMT per particle history. All three spectra were compared to the measured energy spectrum for a ^{137}Cs point source.

Paper II also included a detailed description of the WBC and the low activity laboratory.

1.1.4   Paper III

Published works on the optical transport in GEANT4 and/or GATE usually focus on one specific surface parameter or the study of a specific system [31-40]. The aim in Paper III [24] was to present a more general description of the surface parameter and study their individual and combined impact on an optical transport simulation.

In GEANT4 there are two transport models for optical transport [29], the GLISUR model and the UNIFIED model, develop by Levin and Moisan [41], but only the UNIFIED model is available in GATE. Paper III contained a detailed theory section of how the UNIFIED model is implemented in GEANT4/GATE. The impact of each surface parameter was studied by comparing the change in the optical spectrum with respect to the surface parameter and the results were explained using the UNIFIED model. The optical spectrum was simulated using the model of the WBC presented in Paper II, i.e. Paper III was also a large study of the most suitable surface parameters for the WBC in system II.

Paper III also studied why a simulated energy deposition spectrum for a plastic scintillator in system II showed a full energy peak for high energy gamma-emitting sources, Figure 1, despite the low cross section for photoelectric absorption– less than 1 % for gamma energies above 100 keV [19]. A plastic scintillator is generally not known for its ability to produce full energy peaks and the hypothesis was that, due to the size of the plastic scintillator in system II ($91.5 \times 76.0 \times 25.4$ cm^3), a gamma photon could deposit its entire energy through multiple Compton scatterings. This was studied by looking at the energy deposition and number of Compton scatterings per particle history in plastic scintillator of different sizes for a ^{137}Cs source.

1.1.5   Paper IV

Paper IV [42] was the result of the combined efforts from Paper I – III and presented a Monte Carlo calibration of the WBC in system II.

The most suitable surface parameters for optical transport simulations in the plastic scintillators of the WBC were deduced from the results presented in Paper III. The surface parameters were included in the Monte Carlo model of the WBC presented in Paper II. The model presented in Paper II also included the multiplication in the PMT. Paper IV presented a method to create a PMT spectrum equivalent to a measured energy spectrum with respect to bin/channel size (step 6 in section 1.1). Paper I had shown that a broadening function based only on energy deposition was not suitable for a large plastic scintillator and the Monte Carlo model of the WBC presented in Paper IV included all six steps presented in section 1.1. The Monte Carlo model was verified by comparing the simulated PMT spectrum with the measured energy spectrum for three mono-energetic gamma-emitting point sources.

After the verification, the ICRP (International Commission on Radiological Protection) computational phantoms of the Reference Man and Reference Female were implemented in the Monte Carlo model of the WBC. The PMT spectrum for two source distributions (^{40}K and ^{137}Cs) in the computational phantoms was simulated. Potassium (K) is an important micronutrient that is heterogeneously distributed in the human body and potassium naturally contains small amounts of the radioisotope ^{40}K. The radionuclide ^{137}Cs is often found in emission after accidents at nuclear facilities and accumulates in the body tissues in a similar was as potassium once it has entered the human blood system [43]. ^{40}K and ^{137}Cs were distributed with respect to the potassium content in the ICRP computational phantoms. Hence, the PMT spectrum was the Monte Carlo simulated WBC response for a heterogeneous source distribution in a heterogeneous and anthropomorphic phantom, and this PMT spectrum can be used for a Monte Carlo calibration of the WBC in system II.

2 THEORY

A general, well-written and detailed description of scintillators has been written by Birks [44], which is highly recommended but unfortunately not easily available. Therefore, the main part of the theory section is devoted to a description of the physics processes behind the scintillation in an organic scintillator and the theory is taken from Birks' work unless otherwise stated. The theory for the scintillation process in an organic scintillator requires a quantum mechanical description of the molecular structure of a scintillator. The theory section therefore contains a (very) brief introduction to the quantum theory. A deep knowledge about the scintillation process is not required to understand Paper I – IV, but anyone in the planning stage of making a Monte Carlo simulation of organic scintillators ought to be familiar with what is being simulated.

2.1 Organic scintillators

A scintillator is a substance that emits a characteristic luminescence spectrum of visible or ultraviolet light after it has absorbed energy from an ionizing particle. The properties for a scintillator are quite different deepening on if it is an inorganic or inorganic scintillator. Inorganic scintillators are a favorable choice for gamma-ray spectrometry since they have a higher Z-value and tend to have a better light output and linearity compared to organic scintillators. Organic scintillators have a faster response time compared to inorganic scintillators and are often used for beta spectrometry and fast neutron detection. Paper I – IV presented simulations done for a plastic scintillator, which is an organic scintillator and often the only practical choice for large solid scintillator [23].

2.1.1 A quantum mechanics description of the organic scintillators molecular structure

Schrödinger proposed that the quantization of the hydrogen atom could be explained by treating the bound electron as a standing wave. If the electron is a standing wave then only a certain circular orbits have the circumference that can fit a whole number of wavelengths, other circum-

ferences would lead to a destructive interference of the standing wave and is thus not allowed. If the potential energy of the electron is not time-dependent the hydrogen atom can be descried by the time-independent Schrödinger equation seen in Equation 1.

$$\hat{H}\psi=E\psi \tag{1}$$

$\hat{H}$ is the Hamiltionan operator, E the total energy of the electron and ψ the wave function for the electron in the three-dimensional space (x, y, z). A wave function describes the quantum states of a particle and Equation 1 has several solutions where each solution is an eigenfunction ψ_{nlm}. The eigenfunction describes the behavior of one electron or a pair of electrons in an atom, and an eigenfunction is referred to as an atomic orbital. The size of an orbital is defined as the radius of a sphere in which the probability to find an electron is 90 %, and the probability density for the position of the electron inside an orbital is given by the square of the wave function, $|\psi_{nlm}|^2$.

The eigenfunction ψ_{nlm} is characterized by a set of quantum numbers: n, l, m_l and m_s. The principal quantum number n, an integer value $n = 1,2,3\ldots$, is related to the size and energy of the orbital. A larger orbital, i.e. a larger expectation value of the electron orbit radius, is represented by an increase of n. The angular momentum quantum number l, $l \leq (n-1)$, relates to the shape of the atomic orbital and is denoted by letters where $s = 0$, $p = 1$, $d = 2$, $f = 3$ etc. The magnetic quantum number m_l is an integer value between $-l$ and l and is related to the rotation of the orbital in space relative to the other orbitals in the atom. The spin quantum number m_s describes the spin of an electron within the orbital. An orbital cannot contain more than two electrons and m_s is either -½ or ½. Figure 3 shows the atomic orbital for a hydrogen-like atom described by a wave function up to $2p$.
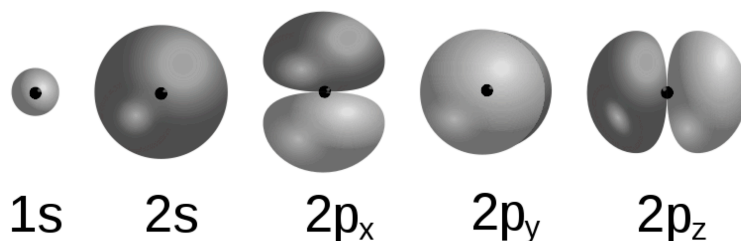
Figure 3. Five images of the atomic orbital for a hydrogen-like atom. The black dot inside each image is the nucleus and the grey spheres are the orbitals. Under each image are the quantum numbers, nl, for the wave function describing the atomic orbital(s). The subscripts x, y and z for the quantum number l refers to the orientation of the orbital in the x, y, z - plane, $m_l = 0$ for x and $m_l = \pm 1$ for y and z. Adapted image taken from Wikipedia Commons [b].

More specific about the organic scintillators

An organic compound contains carbon and its molecular structure greatly depends on the structure of the carbon atom. The ground state for carbon is $1s^2\ 2s^2 2p^2$ where $1s$, $2s$ and $2p$ are nl and the exponentiations are the number of electrons in each orbital.

The electron in the $2s$ orbital can be excited to the $2p$ orbital, and the carbon atom is prepared for binding when it is in the $1s^2\ 2s^1 2p^3$ state. The orbital for $n = 2$ now contains four valence electrons which are mixed into new orbitals called hybridized orbitals. There are three possible configurations for the hybridized orbitals, tetrahedral, trigonal and linear, and the latter two are luminescent.

The tetrahedral configuration, sp^3 hybridization

In a tetrahedral configuration four orbitals, one s and three $2p$ orbitals, are hybridized into four equivalent orbitals. An example of this can be found in methane where a hydrogen atom is bound to each of the four valence electrons in the carbon atom. Figure 4 shows the methane molecule (left) and the four hybridized orbitals (right). Tetrahedral molecules are not luminescent.
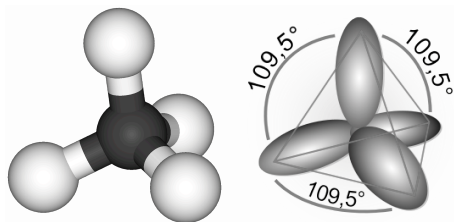
Figure 4. To the left is the tetrahedral molecule methane where four hydrogen atoms (white) are bound to the carbon atom (black). To the right are the four hybridized orbitals in methane shown. The bound angles between the electron bonds are 109.5°. Adapted images taken from Wikipedia Commons [(c)].

The trigonal configuration, sp^2 hybridization

In a trigonal configuration one of the carbon p-orbitals is unchanged and the remaining three are hybridized. For exampled, p_z remains unchanged and three equivalent hybrid-orbitals, sp^2, are created by mixing s, p_x and p_y. The sp^2-orbitals are in the same xy-plane with a bond angle of 120°. The unchanged orbital is called π-electron and is mirror symmetric; in the example above p_z is the π-electron and it is mirror symmetric in the xy-plane. An example of a trigonal configuration is shown in Figure 5.

The trigonal configuration is found in the benzene molecule where six carbon atoms, each in a trigonal configuration, are bound together in a ring structure by σ-bonds (a covalent bond symmetrical about the bond axis) between the carbon atoms. The benzene molecules can then bind to each other through the π-electrons, i.e. a π-bond. Figure 6 shows the structure of the benzene molecules (left) where each carbon atom has a π-electron in the xy-plane (middle), which makes it possible for benzene molecules to bind through π-bonds (right). The π-electrons are delocalized, meaning they do not belong to a single bond/atom but rather to a group of atoms, which in general makes the molecule more stable as it lowers the overall energy of the molecule. An excited π-electron can deexcite through luminescence, hence an organic material where the carbon atoms are in a trigonal configurations can be used as a scintillator.
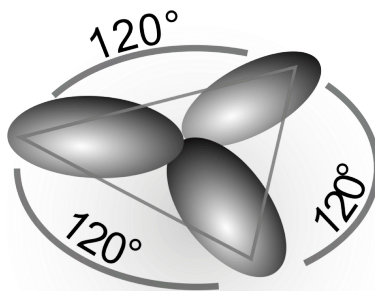
Figure 5. The sp^2 hybridization, all three orbitals are in the same plane and the bond angles are 120°. Adapted images taken from Wikipedia Commons [d].
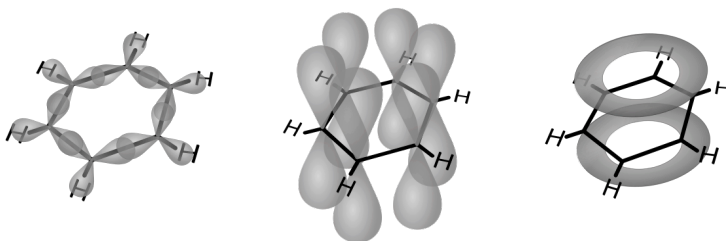
Figure 6. To the right is a benzene molecule; the sp^2 orbitals are the xy-plane. In the middle is a benzene ring and with the 6 p_z orbitals depicted. To the right are two benzene molecules, bound at the π-electrons, depicted. Adapted images taken from Wikipedia Commons [e].

The linear configuration, sp hybridization

In a linear configuration two p-orbitals remain unchanged. If for example p_y and p_z remain unchanged then s and p_x form two equivalent hybridized orbitals with bond angle 180° along the x-axis. Linear configurations can be found in acetylene seen in Figure 7. Acetylene has two carbon atoms and each carbon atom binds one hydrogen atom by a σ-bond. The carbon atoms are bound to each other by two π-bonds and one σ-bond. As for the trigonal configuration is it the excitation and following deexcitation of π-electrons that gives rise to luminescence.

Figure 7. The acetylene molecule, which consists of two *sp* hybridized carbon atoms (black). To each carbon atom a hydrogen atom (white) is bound through a σ-bond and the bonds between the carbon atoms are two π-bonds and one σ-bond. Adapted images taken from Wikipedia Commons [f].
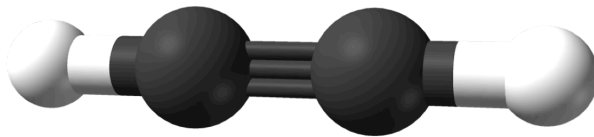
2.1.2 The excitation and deexcitation of π-electrons in organic scintillators

The energy levels for a π-electron in an organic molecule are shown in Figure 8. The singlet states, total spin 0, are labeled S_0, S_1 and S_2 and the triplet states, total spin 1, are labeled T_1 and T_2. The molecule ground state is denoted S_{00} and the finer levels in each state: S_{10}, S_{11}, S_{12}, … and T_{10}, T_{11}, T_{12}, … are vibrational states. Organic molecules used as scintillators have a gap of 3-4 eV between S_0 and S_1 and about 0.15 eV between the vibrational states. In room temperature the average thermal energy is 0.025 eV and nearly all molecules are in the ground state S_{00}. The electron configuration can be excited into any number of states when kinetic energy is absorbed from a charged particle passing nearby. An excited electron in the higher states will within picoseconds dexcite to some of the vibrational levels in S_1 through non-radiative internal conversion. An electron in the vibrational stages, S_{11}, $S_{12...}$, are not in thermal equilibrium with its neighbors and will quickly loose the excess of vibrational energy through non-radiative transitions. Hence, short after energy has been absorbed there is a population of excited molecules in the S_{10} state. Luminance occurs when a π-electron deexcites from the S_{10} to S_0 state, or from T_{10} to S_0.
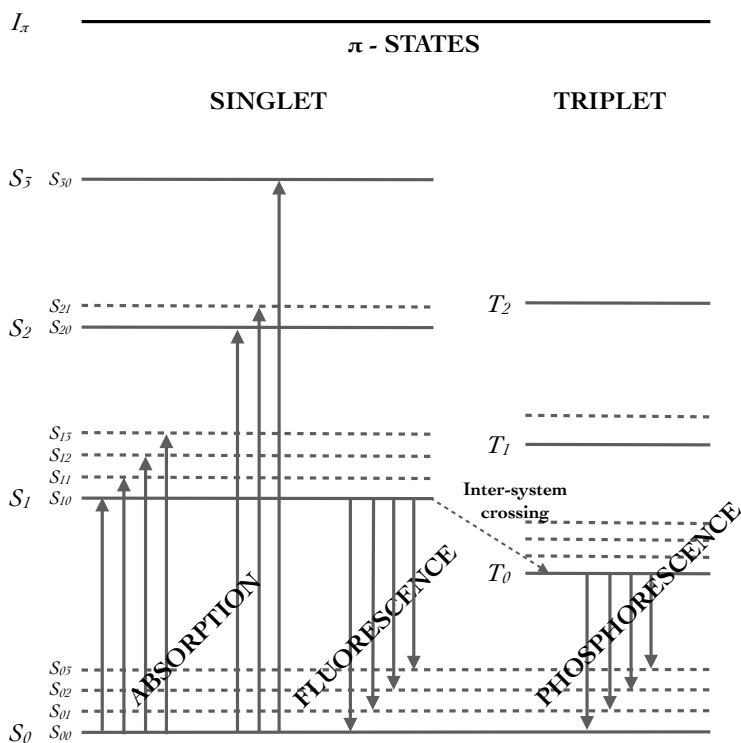
Figure 8. The π-electron energy levels in an organic molecule. S_{00} is the ground state and S_1, S_2, and S_3 are excited singlet states and S_{01}, S_{02}, S_{21},…etc. are vibrational energy sub-levels. T_1, T_2, and T_3 are excited triplet states. I_{π} is the ionization energy for the π-electron. Redrawn from Birks [g].

The luminescence process can be divided into three parts: fluorescence, phosphorescence and delayed fluorescence. Fluorescence is the prompt emission of light following excitation and is described by Equation 2.

$$I = I_0 e^{-(t/\tau)} \qquad (2)$$

I is the fluorescence intensity at a time t and τ is the fluorescent decay time for S_{10}, usually a few nanoseconds. Phosphorescence originates from when an excited singlet state is converted into a triplet state through inter-system crossings. The lifetime for the triplet state can be as long as 10^{-3} s and the emitted light have a longer emission time and longer wavelength compared to light emitted through fluorescence. Delayed fluorescence originates from when a electron in the T_1 state is thermally excited back to

the S_1 state and from there deexcites to the S_0 state. The emission spectrum is the same as for fluorescence but with a longer emission time, hence the term delayed fluorescence. A good scintillator should convert a large fraction of the incoming energy to prompt fluorescence while minimizing the contributions from phosphorescence and delayed fluorescence. When a charged particle deposits energy in a scintillating material only a small fraction, ~ 4 %, of the deposited energy will be converted to fluorescent photons, this is defined as the absolute scintillation efficiency $\varepsilon_{AbsSci.}$ The remaining energy is dissipated through non-radiative processes, mainly heat, and are referred to as quenching.

There are six principal types of organic scintillators, which are separated by the number of constituents in the scintillation material:

Unitary systems (1-component system)

> Pure crystals, for example anthracene

Binary system (2-component systems)

> Liquid solutions
> Plastic solutions
> Crystal solution

Ternary systems (3-component systems)

> Liquid solutions
> Plastic solutions

In a 1-component system the emission spectrum ≈ the absorption spectrum. As seen in Figure 8, a fluorescent photon can be absorbed and re-radiated with a longer wavelength by the scintillating material, which result in a small shift of the emission spectrum compared to the absorption spectrum. In a 2-component system an efficient scintillator is added to a bulk solvent. The excitation energy undergoes substantial energy transfers from molecule to molecule in almost all organic materials before deexcitation. Energy absorbed by the bulk solvent will eventually be transferred to an efficient scintillator molecule that deexcites through luminescence. In a 3-component system a third component is added. Its function is to absorb the luminescent light emitted by the primary scintillating molecules and then re-radiate light with a longer wavelength. This can be used for matching the sensitivity of a photocathode or to minimize bulk absorption in large liquid or plastic scintillators.

2.1.3   Light output and Birks' formula

For fast electrons, above 125 keV, the light yield from a scintillator is linear and can be described by Equation 3 and 4 [23]. Fast electrons have a low specific energy loss, $\partial E/\partial r$, unit MeV/(mg cm^{-2}) (the particle range r in the scintillator is expressed in mg cm^{-2}), and thus the molecular excitations and ionizations are spaced several molecular distances apart along the particle track. Interactions between molecules are negligible and the scintillation response L, the energy emitted as fluorescence light, is proportional to the deposited energy in the scintillator, E. The relationship between L and E is seen in Equation 3, where ε_{AbsSci} is the absolute scintillation efficiency mentioned in the previous section.

$$L = \varepsilon_{AbsSci} E \qquad (3)$$

Equation 3 can be written in a differential form, see Equation 4. The term $\partial L/\partial r$, unit MeV/(mg cm^{-2}), is the specific fluorescence.

$$\frac{\partial L}{\partial r} = \varepsilon_{AbsSci} \frac{\partial E}{\partial r} \qquad (4)$$

For heavier particles or slow electrons with energies below 125 keV, L will increase nonlinearly with E. This is not accounted for in Equation 3 and 4 and for such cases the empirical Birks' formula is widely used. Birks assumed that the high ionizing density along the track of a charged particle would result in a quenching of the primary excitation caused by damaged molecules and this would result in a decrease of the absolute scintillation efficiency ε_{AbsSci}. Birks further assumed that the specific density of damaged molecules is directly proportional to the ionizing density, which can be expressed with $B(\partial E/\partial r)$ where B is proportionality constant. Further, if only a fraction k of the damaged molecules are involved in the quenching process and if the quenching can be considered unimolecular, then $\partial L/\partial r$ can then be expressed with Equation 5, which is referred to as Birks' formula.

$$\frac{\partial L}{\partial r} = \varepsilon_{AbsSci} \frac{\partial E}{\partial r} \left(1 + kB \frac{\partial E}{\partial r} \right)^{-1} \qquad (5)$$

Notice, if $kB \to 0$, that is if the ionizing density is low and/or few molecules are involved in the quenching process, then Equation 5 $\to$ Equation 4. Birks' formula can be rewritten into Equation 6.

$$\frac{\partial L}{\partial E} = \varepsilon_{AbsSci} \left(1 + kB \frac{\partial E}{\partial r} \right)^{-1} \qquad (6)$$

The constants kB, unit mg cm^{-2} MeV^{-1}, are often referred to as Birks' constant, which is treated as a single and adjustable parameter when fitting experimental data to Birks' formula and the parameter ε_{AbsSci} then gives the absolute normalization [23].

2.1.4 The plastic scintillator NE 102A

The plastic scintillators presented in Paper I – IV are made of NE 102A, which is a 3-component general-purpose organic scintillator. The product name is now obsolete but the material is equivalent to the commercially available BC-400 (Saint-Gobain Crystals, USA) and EJ-212 (ELJEN Technology, USA) [23].

The predecessor to NE 102A is NE 102, and NE 102 has the following composition: ~ 97 % PVT (polyvinyltoulene), ~ 3% PT (p-terphenyl) and 0.05% POPOP (p-bis (2-5-phenyloxazolyl)benzene) [45]. The difference between NE 102 and NE 102A has not been found in the literature, but the density for both NE 102 and NE 102A is 1.032 g/cm^3 [46, 47]. There is no difference in the emission spectra and decay times between NE 102 and NE 102A [48] and the physical data for NE 102 [49] matches the data for NE 102A [46] . Hence, the composition of NE 102 and NE 102A is most likely the same or very similar.

2.1.5 ICRP computational phantoms

The ICRP computational phantoms [50] are made from segmented whole body computed tomography image sets of a male and a female in a supine position. Segmentation means that each pixel value in an image is given an organ identification number. Coupled to each identification number is an assigned tissue with an elemental composition given in mass percentage. The image slice refers to an anatomical thickness given by the slice thickness and each pixel defines a volume element, i.e. a voxel. The Reference Male contains 1,946,375 voxels in a 254 × 127 × 222 array (voxel volume

36.54 mm^3) and the Reference Female phantom contains 3,886,020 voxels in a 299 × 137 × 348 array (voxel volume 15.25 mm^3). The ICRP computational phantoms are in the shape of a cuboid and the voxels not associated to a tissue are filled with air. The image sets have been scaled to fit the reference values for the Reference Male (1.76 m and 73.0 kg) and the Reference Female (1.63 m and 60.0 kg) defined by ICRP [51]. ICRP uses the term computational phantom and this terminology has been adapted in this thesis, another commonly used term is voxel phantoms.

3 METHOD

3.1 The geometrical Monte Carlo model of the WBC in system II

The whole body counter (WBC) in system II consists of four equivalent detectors. Two detectors are placed above a patient bed and two below and the distance between the patient bed and the upper two detectors is variable. Figure 9a shows a schematic of the WBC and Figure 9b shows detector 1 from above. In Paper II – IV the WBC response for a gamma-emitting point source was simulated (section 3.3.1 – 3.3.4) and the source was placed on the patient bed at three positions indicated with ✖ in Figure 9(a-b). Figure 9c shows the position of the ICRP computational phantom (section 3.3.5).
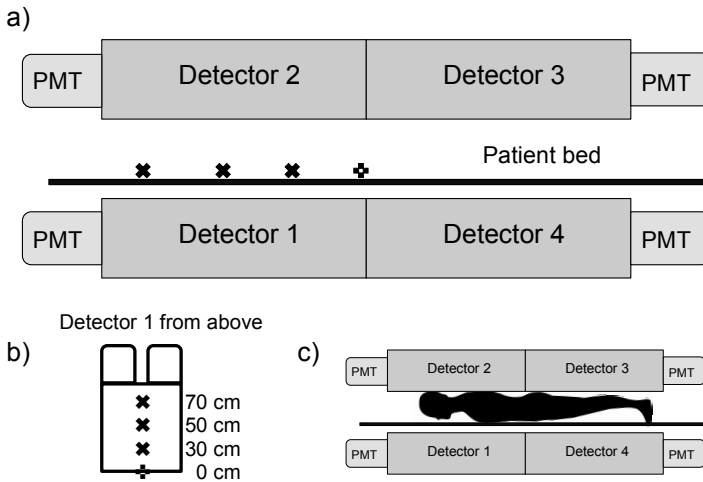
Figure 9(a-c). a) A schematic of the WBC system. All four detector are equivalent and inside each detector is a plastic scintillator measuring 91.5 × 76.0 × 25.4 cm^3. b) A schematic of the PMT placement and the source positions relative detector 1. Two PMT are mounted through a perspex lightguide on each plastic scintillator, in total there are eight PMT in the WBC system. The source was placed on the patient bed. c) A schematics of the WBC and the position of the ICRP computational phantom.

Inside each detector is a plastic scintillator (NE 102A equivalent to BC-400 [23, 46]), measuring 91.5 × 76.0 × 25.4 cm^3. On one of the plastic scintillator short ends two 12″ (30.5 cm) photomultiplier tubes (PMT, model EMI 9545A) are mounted through a 16.5 cm long perspex lightguide. A reflecting aluminum foil is placed on the plastic scintillator short end opposite the PMT. The signals from the PMT are added and then amplified detector-wise (Canberra Amplifier 816A)[1]. The signal from all four detectors can be summed or fed individually into an Ortec pulse-height analyzer (Ortec ASPEC-927). The plastic scintillator, the lightguide and the coupling between the lightguide and PMT are inside a detector housing with a 0.397 mm copper window facing the patient bed. Figure 10 and Figure 11 show the Monte Carlo model, defined in Paper I, of a detector. All measurements were taken from the WBC system in Figure 9.
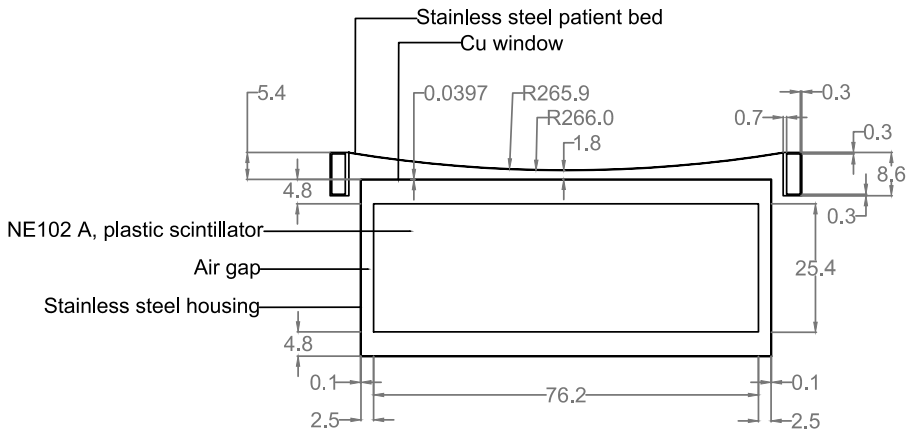

Figure 10. The latitudinal cross-section of a detector and patient bed. All dimensions are given in cm.

[1] The electronics have been replaced and the PMT are now amplified individually before the signals are summarized.
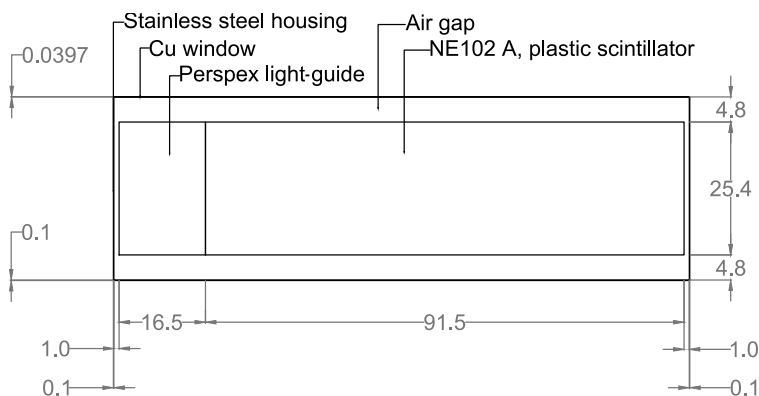
Figure 11. The longitudinal cross-section of a detector. All dimensions are given in cm.

In Paper I the WBC response was modeled using the Monte Carlo code MCNPX 2.6.0. The model of the WBC used in Paper I is referred to as the MCNPX mode throughout the thesis. The MCNPX model consisted of four equivalent detectors and the patient bed as shown in Figure 10 and Figure 11. The walls in the twin steel chamber have a 3 mm lead coating; the lead coating was included in the MCNPX model. The lightguides were modeled as a block made of poly(methyl mechacrylate) (PMMA). The PMT were not included in the model.

In Paper II – IV the WBC response was modeled using the Monte Carlo code GATE. In Paper II GATE v6.1 (using the GEANT4 9.4 p03 libraries) was used and in Paper III –IV GATE v6.2 (using the Geant4 9.5 p01 libraries). The model of the WBC in Paper II – IV is referred to as the GATE model throughout the thesis. The GATE model was based on the MCNPX model but with a few modifications, the patient bed suspension and the lead coating were not included. The lightguides were omitted and the detector housing was shortened with 16.5 cm in the longitudinal direction. Instead of the light guides a volume measuring $2.5 \cdot 10^{-6} \times 76.0 \times 25.4$ cm^3, representing a photocathode, was placed directly on the plastic scintillator short end. On the other short end of the plastic scintillator a volume representing the reflecting aluminum foil was placed. The aluminum foil volume measured $0.012 \times 76.0 \times 25.4$ cm^3, the thickness 0.012 cm was taken from the data for 3M^{TM} Aluminium Foil Tape 425 [38]. In both the MCNPX model and the GATE model the plastic scintillator properties were taken from the data for BC-400 [46].

23

All four detectors are equivalent and in section 3.3.1 – 3.3.4 the response was simulated only for detector 1. The response from each individual detector was simulated when the ICRP computational phantoms were implemented in the GATE model, section 3.3.5.

3.2 Paper I

3.2.1 Achieving a simulated total efficiency equivalent to a measured total efficiency

The measured total efficiency (cps Bq^{-1}) for a ^{137}Cs point source was compared to the simulated total efficiency. The simulated total efficiency was given by sum of all scored particle histories in detector 1 divided by the number of source particles.

Measurements

A ^{137}Cs button source (4.7 kBq ± 5 %) was placed on the patient bed and moved in the longitudinal and latitudinal direction in steps of 10 cm, a total of 77 source positions. At each source position the energy spectrum was recorded in 512 channels using detector 1. Channels 1 – 8 was discriminated due to noise. The measurement time was 5 minutes. The measured data presented in this thesis is not the same as presented in Paper I. The measured data presented in this thesis was obtained using the same method, geometry and radionuclide as in Paper I, but the measurement was increased to achieve a lower uncertainty.

Simulations

A ^{137}Cs (modeled as a mono-energetic gamma-emitter with energy 661.657 keV) point source was placed at the corresponding positions in the MCNPX model of the WBC. The energy deposition spectrum was scored for the plastic scintillator in detector 1 using the MCNPX f8 tally. The spectrum resolution was set to 10 keV and 10^7 source particles were run.

Discrimination level

To compare the simulated total efficiency with the measured total efficiency the same discrimination as in the measurements needed to be applied to the simulated energy deposition spectrum. However, a plastic scintillator

cannot be energy calibrated due to the poor resolution. This was solved as follows; the measured total efficiency was calculated at each source position. The simulated total efficiency was calculated using all scored particle histories in the simulated energy deposition spectrum[2]. The simulated total efficiency was compared to the measured total efficiency at each source position. Then one by one, starting from the lowest energy bin, the counts in the lowest energy bin was excluded from the calculation of the simulated total efficiency, i.e. low energy contributions were discriminated. For each new discriminated energy bin the simulated total efficiency was compared with the measured total efficiency at all *77* source positions. The discrimination level that gave the best agreement between the measured total efficiency and the simulated total efficiency with respect to all source positions was used as a discrimination level when calculating the simulated total efficiency.

3.2.2   Study the impact of a nonlinear light yield

A spectrum of emitted light for a linear light yield was obtained by simulating the energy deposition spectrum with bin size 0.001 MeV and setting the deposited energy in MeV equal to MeVee for all bins. This is referred to as the linear light yield spectrum.

A nonlinear light yield was simulated using the f8 PHL (pulse height light) tally, which calculates the emitted light, unit MeVee, per particle history. For the f8 PHL tally the user must provide $\partial L/\partial E$ (emitted fluorescent light per deposited energy) in Equation 6. All terms in Equation 6 were available [52, 53], except for Birks' constant kB, for which several values have been reported [54, 55]. A value for kB was determined by calculating $\partial L/\partial E$ for 11 values of kB, ranging from 9.0 to 10 mg cm^{-2} MeV^{-1} in steps of 0.1 mg cm^{-2} MeV^{-1}. The 11 sets of $\partial L/\partial E$ (one for each kB) were used as an input parameter for the f8 PHL tally to calculate the spectrum

---

[2] Except for the 0 – 10^{-6} MeV bin that should always be defined for the f8 tally but the result should not be used. A source particle not passing a volume and a source particle that pass a volume but without depositing any energy is differentiated in MCNPX by an arbitrary energy loss of 10^{-12} MeV for a source particle passing the volume. These particles are scored in the 0 – 10^{-6} MeV bin [18].

of emitted light in MeVee. This is referred to as the nonlinear light yield spectrum.

A linear and nonlinear light yield spectrum was simulated for a ^{137}Cs source. According to the theory presented in section 2.1.3, the light yield for a gamma photon with energy 661.657 keV depositing its entire energy through photoelectric absorption (unlikely but possible, see Paper III) is linear. That is, the number of counts in the bin for full energy absorption, 0.662 MeVee, in the nonlinear light yield spectrum should be equal to the number of counts in the 0.662 MeVee bin in the linear light yield spectrum. The correct value for *kB* was defined as the *kB* used to calculate *∂L/∂E* that fulfilled this condition.

Once *kB* had been determined a linear light yield spectrum and a nonlinear light yield spectrum was simulated for a ^{65}Zn point source (modeled as a mono-energetic gamma-emitter with energy 1115.546 keV). ^{65}Zn was used to get a broader range of electron energies due to more multiple Compton scatterings compared to for a ^{137}Cs source.

3.3 Paper II – Paper IV

The methods for Paper II –IV are grouped together and divided into five mayor parts.

A. The origin of the full energy peak in a simulated energy deposition spectrum from a plastic scintillator obtained for high-energy mono-energetic gamma-emitting sources was studied (Paper III).

B. The surfaces needed for optical transport were defined in the GATE model (Paper II). Different surface parameters were tested to find the most appropriate for the WBC system (Paper III).

C. The PMT multiplication was included in the GATE model (first presented in Paper II, but a more detailed description was given in Paper IV).

D. The GATE model of the WBC system was verified by comparing measured energy spectrum to simulated PMT spectrum (Paper IV).

E. The ICRP Computational Phantom for the Reference Male and Reference Female was included in the GATE model (Paper IV).

3.3.1 A. The origin of the full energy peak

The origin of the full peak in an energy deposition spectrum was studied by looking at the energy deposition by a ^{137}Cs source (modeled as a mono-energetic gamma-emitter with energy 661.657 keV) in a plastic scintillator (BC-400) in the shape of a cylinder. In this thesis the results for two cylinder sizes are presented, one with radius 1 cm and height 2 cm and one with radius 20 cm and height 40 cm. For both cylinders the total energy deposition spectrum and five energy deposition spectra with respect to the number of Compton scatterings were scored.

3.3.2 B. Definition of the surfaces in the GATE model

The geometrical GATE model, described in section 3.1, was used in all simulations. The material parameters that are needed for generation and transport of optical photons were taken from the literature and are presented in Paper III. To define the physics processes for an optical photon at the plastic scintillator boundaries three surfaces were defined:

- The plastic scintillator surface. Defined the plastic scintillator surface at the scintillator – air interface.
- The photocathode surface. Defined the photocathode placed at the one of the plastic scintillator short ends. This surface scored the number of detected optical photons per particle history.
- The aluminum foil surface. Defined the aluminum foil placed on the plastic scintillator short end opposite the photocathode surface.

Each surface was defined by a set of surface parameters, a description of each surface parameter and the physics processes it controls are described in Paper III.

156 simulations were performed for a ^{65}Zn point source (modeled as a mono-energetic gamma-emitter with energy 1115.546 keV; 10^6 source particles were run in each simulation. The energy deposition in the plastic scintillator, the following optical transport and the detection of optical

photons by the photocathode surface was simulated. The impact of each surface parameter was studied by comparing the optical spectrum with respect to surface parameter and source position, see Figure 9b for source positions.

3.3.3   C. The PMT multiplication

The WBC has two PMT coupled to each scintillator, see Figure 9b. The PMT converts the optical photons to an amplified electric signal as follows. An optical photon undergoes photoelectric absorption at the PMT photocathode and a photoelectron is emitted, the photoelectron reaches the PMT dynode chain and undergoes multiplication (steps 3 – 5 in section 1.1). The PMT gain, G, and its relative standard deviation, σ_G/G, are given by Equation 7 and Equation 8, respectively [23].

$$G = A\delta^n \tag{7}$$

$$\sigma_G / G = 1 / (1 - \delta) \tag{8}$$

A is the fraction of photoelectrons reaching the first dynode, n is the number of dynodes and δ is the number of released electrons at each dynode per incoming electron.

Equation 7 shows that the G depends on a series of multiplicative events. A variable which is the product of positive and independent variables can be described by a lognormal distribution [56]. It was assumed that the multiplication processes in the PMT were independent of each other and that G was lognormally distributed, i.e. $\ln(G)$ is normally distributed, where the expectation value $E[G]$ and the variance $Var[G]$ were given by Equation 7 and Equation 8, respectively. $E[G]$ and $Var[G]$ were calculated for $A = 1$, $n = 11$ and $\delta = 5$, 5.5 and 6. The number of dynodes in the PMT EMI 9545A is 11 [57], A is often close to 1 and the value for δ is unknown but a common value is $\delta = 5$ [23]. $E[G]$ and $Var[G]$ were then used to calculate the mean, μ, and standard deviation, σ, for $\ln(G)$ using equation 9 and Equation 10, respectively.

$$\mu = \ln(E[X]) - \frac{1}{2}\ln\left(1 + \frac{Var[X]}{(E[X])^2}\right) \tag{9}$$

$$\sigma = \sqrt{\ln\left(1 + \frac{Var[X]}{(E[X])^2}\right)} \qquad (10)$$

A vector of detected optical photons by the photocathode surface per particle history was given by GATE. This was used as an input to the MATLAB model of the PMT. The MATLAB model described the PMT in the following way; one detected optical photon produced one photoelectron that reached the first dynode and underwent multiplication. All photoelectrons per particle history had the same gain factor. All particle histories had a different gain factor sampled from a lognormal distribution.

For each entry in the output vector from GATE a gain factor, $G_{logninv}$, was sampled from the inverse of the cumulative lognormal distribution for $\ln(G)$ described by μ and σ. The number of generated electrons per particle history was calculated using $G_{logninv}$. The output from MATLAB was a vector with the number of generated electrons per particle history. The spectrum made from the vector was referred to as the PMT spectrum.

3.3.4   D. Verification of the GATE model of the WBC system

Based on the work in Paper III the surface parameters in the GATE model could be defined.

The plastic scintillator surface parameters were: dielectric-dielectric, ground, σ_α =6°, reflectivity = 1.0 and specular lobe = 1.0. I.e. the plastic scintillator surface described a scintillator with a rough surface in direct contact with the surrounding air[3] (given by ground and σ_α =6°). Optical photons reaching the plastic scintillator surface could be refracted into the air layer (given by dielectric-dielectric) and no optical photons were absorbed by the surface itself (given by reflectivity = 1.0). The reflectivity and refraction were simulated with respect to the surface roughness (given by specular lobe = 1.0).

The aluminum foil surface parameters were: dielectric-metal, polished and reflectivity = 1.0. I.e. the aluminum foil surface was described as a metallic surface in direct contact with the plastic scintillator and no optical photons were refracted (given by dielectric-metal). No optical photons

---

[3] As shown in Figure 10 and Figure 11, there is an air layer between the plastic scintillator and the detector housing.

were absorbed by the surface itself (given by reflectivity = 1.0). Hence all optical photons were reflected. The reflection angle was equal to the incident angle (given by polished).

The photocathode surface parameters were: dielectric-metal, polished, reflectivity = 0 and efficiency = quantum efficiency for the PMT EMI 9545A [57]. I.e. the photocathode surface was described as a metallic surface in direct contact with the photocathode volume and no optical photons were refracted (given by dielectric-metal). All optical photons were absorbed by the surface itself (given by reflectivity = 0) and the optical photons were detected with the same probability as in the PMT EMI 9545A.

Set-up for the verification
The GATE model was verified by comparing the measured energy spectrum with the PMT spectrum. The energy spectrum was measured for three button sources of ^{137}Cs ($0.19 \cdot 10^6$ Bq ± 3.7 %), ^{54}Mn ($1.9 \cdot 10^3$ Bq ± 5 %) and ^{65}Zn ($0.77 \cdot 10^3$ Bq ± 5 %), placed at source positions 30 cm, 50 cm and 70 cm, see Figure 9b. This was compared to the PMT spectrum simulated for mono-energetic gamma-emitting point sources of energy 661.657 keV (^{137}Cs), 834.848 keV (^{54}Mn) and 1115.546 keV (^{65}Zn) at the same position in the WBC model. 10^6 source particles were run for each nuclide.

Bin size of the PMT spectrum and optical spectrum
When making the PMT spectrum the bin size was determined as follows. The channel number C_{max} for the peak maximum on the x-axis in the measured energy spectrum at source position 70 cm was determined for each nuclide. The PMT spectrum was created from the vector of generated electrons per particle history using the MATLAB function `histc`. The number of bins in the PMT spectrum for each nuclide at source position 70 cm was chosen so that the bin number for the peak maximum on the x-axis was equal to C_{max}. This gave three bin sizes, one for each nuclide, the mean of the three bin sizes was calculated and the mean bin size was used for creating the PMT spectrum for all nuclides at each source position. The same approach was used for the optical spectrum.

3.3.5 E. The ICRP Computational Phantom for the Reference Male and Reference Female

The ICRP computational phantoms of the Reference Male and Reference Female were implemented in the GATE model described in section 3.1 and section 3.3.4. The WBC response was simulated for a heterogeneous radionuclide distribution of ^{40}K and ^{137}Cs, respectively.

The position of the computational phantoms in the WBC is shown in Figure 9c. In a WBC measurement the body is in a prone position. Therefore, the computational phantoms were inverted, i.e. the ventral surface was facing the patient bed, with the anterior above detector 1. A detailed description of the position of the computational phantom with respect to the patient bed and detector 2 and detector 3 are given in Paper IV.

The number of source particles in a voxelized source is defined per voxel. The mass percentage of potassium in the ICRP computational phantoms varies from 0 % to 0.4% and voxels with potassium content 0.1 % was assigned 1 source particle, 0.2 % was assigned 2 source particles and so on. This resulted in $3.896 \cdot 10^6$ source particles for the Reference Male and $6.071 \cdot 10^6$ for the Reference Female. The difference in source particles is due to the different number of voxels in each phantom, see section 2.1.5, and the simulated results for the Reference Female were scaled to correspond to the same number of source particles as for the Reference Male.

The same source distribution was used for ^{40}K and ^{137}Cs, ^{137}Cs accumulates in the human body in a similar way as potassium once it has entered the blood system according to the ICRP's biokinetic model [43]. Each source particle was defined as a mono-energetic gamma-emitter with energy 1460.830 keV for ^{40}K and 661.657 keV for ^{137}Cs. The PMT spectrum was simulated for each detector in the WBC and the individual PMT spectra was summarized to create one single PMT spectrum from all four detectors.

For the Reference Female the summed PMT spectrum for a source distribution of both ^{40}K and ^{137}Cs was calculated. This was done for two different source distributions, one where the number of source particles for ^{40}K was equal to the number of source particles for ^{137}Cs and one where the counts in the PMT spectrum for ^{40}K were scaled with 0.1, i.e. as if the number of source particles was 10 times higher for ^{137}Cs.

4   RESULTS

4.1   Paper I

4.1.1   Achieving a simulated total efficiency equivalent to a measured total efficiency

The Monte Carlo simulated total efficiency and the measured total efficiency for a ^{137}Cs point source are shown in Figure 12 and Figure 13. All measurements and simulations were performed using detector 1. The dead time in the measurements was less than 5 %. Figure 12 shows the results for when the source was placed on the patient bed and moved along the WBC long side. The source positions 30 cm, 50 cm and 70 cm on the x-axis above "Detector 1" are also shown in Figure 9b. Figure 13 shows the results for when the source was placed at source position 0 cm and 60 cm in Figure 9b and moved across detector 1. The negative x-axis in Figure 13 shows the results for the right side of detector 1 in Figure 9b. The discrimination level in the simulations was 190 keV. The results show a good agreement between simulated total efficiency and measured total efficiency for all source positions except close to the edges of the plastic scintillator, source position 0 cm in both Figure 12 and Figure 13.

4.1.2   Study the impact of a nonlinear light yield

The correct value for kB was defined as the kB used to calculate $\partial L/\partial E$ that, when used as an input in the f8 PHL tally, gave an equal number of counts in the 0.662 MeVee bin for both the nonlinear light yield spectrum and the linear light yield spectrum obtained for a ^{137}Cs source. This was fulfilled for kB = 9.6 mg cm^2 MeV^{-1}. The nonlinear light yield, using kB = 9.6 mg cm^{-2}MeV^{-1}, was simulated for a ^{65}Zn source. No difference was found between the nonlinear light yield spectrum and the linear light yield spectrum.
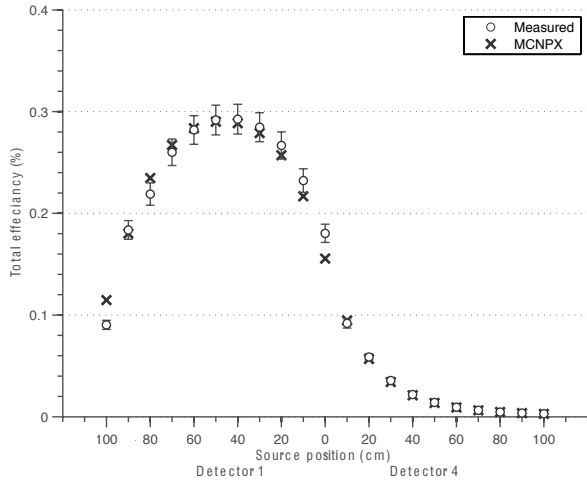
Figure 12. The Monte Carlo simulated total efficiency (labeled MCNPX) and the measured total efficiency for a ^{137}Cs point source. All results were obtained using detector 1 in Figure 9b. The uncertainty for the simulated total efficiency is too low to be depicted in the figure.

Figure 13. The Monte Carlo simulated total efficiency (labeled MCNPX) and the measured total efficiency for a ^{137}Cs point source. All results were obtained using detector 1 in Figure 9b. The uncertainty for the simulated total efficiency is too low to be depicted in the figure.
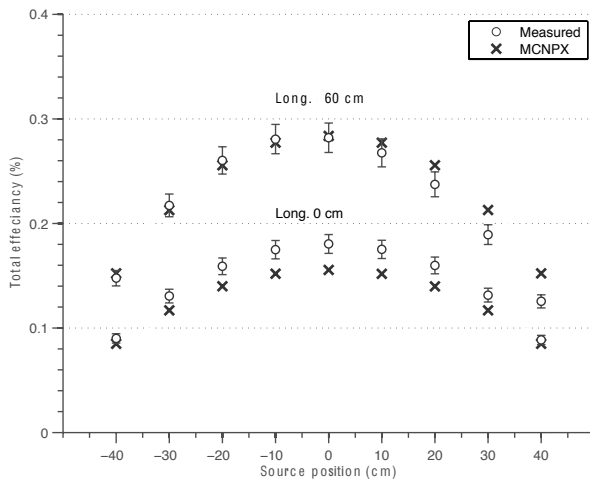
33

4.2 Paper II – IV

4.2.1 A. The origin of the full energy peak

Figure 14 shows the total energy deposition spectrum and five energy deposition spectra, with respect to the number of scored Compton scatterings, for a ^{137}Cs source in two plastic scintillators of different sizes. The total energy deposition spectrum shows the scored deposited energy per particle history. The energy deposition spectrum with respect to Compton scatterings shows the scored deposited energy for particle histories with a specific number or interval of scored Compton events.
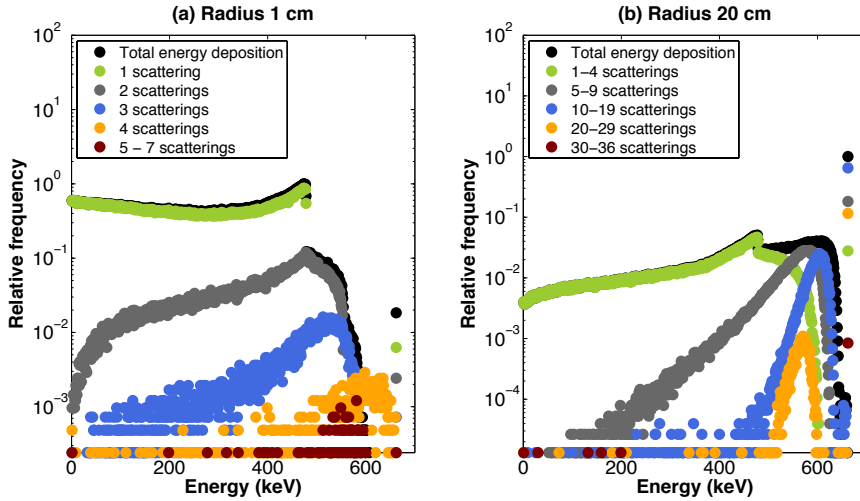

Figure 14(a-b). a) The energy deposition spectrum for a ^{137}Cs source obtained for a plastic scintillator in the shape of a cylinder with radius 1 cm and height 2 cm. b) The energy deposition spectrum for a ^{137}Cs source obtained for a plastic scintillator in the shape of a cylinder with radius 20 cm and height 40 cm. Notice, the y-axis shows the relative frequency, not counts.

4.2.2 B. Definition of the surfaces in the GATE model

Paper III presented a large summary of the surface parameters and their impact on the optical transport simulations and the optical spectrum. Figure 15 shows an example of one of the most important surface parameters,

surface finish. The surface finish controls if an optical photon can be refracted at the surface boundary. Together with two other surface parameters (reflectivity type and σ_α) it also controls the probability for either reflection or refraction and the reflection or refraction angle.

The optical spectrum in Figure 15 was obtained for four different surface finishes for the plastic scintillator surface: polished (P) polished-front-painted (PFP), ground (G) and ground-front-painted (GFP). For each surface finish the optical spectrum was simulated at three source position, 30 cm, 50 cm and 70 cm. The impact on the optical transport was studied by looking at the shift in the optical spectrum – the change of the maximum peak position on the x-axis.
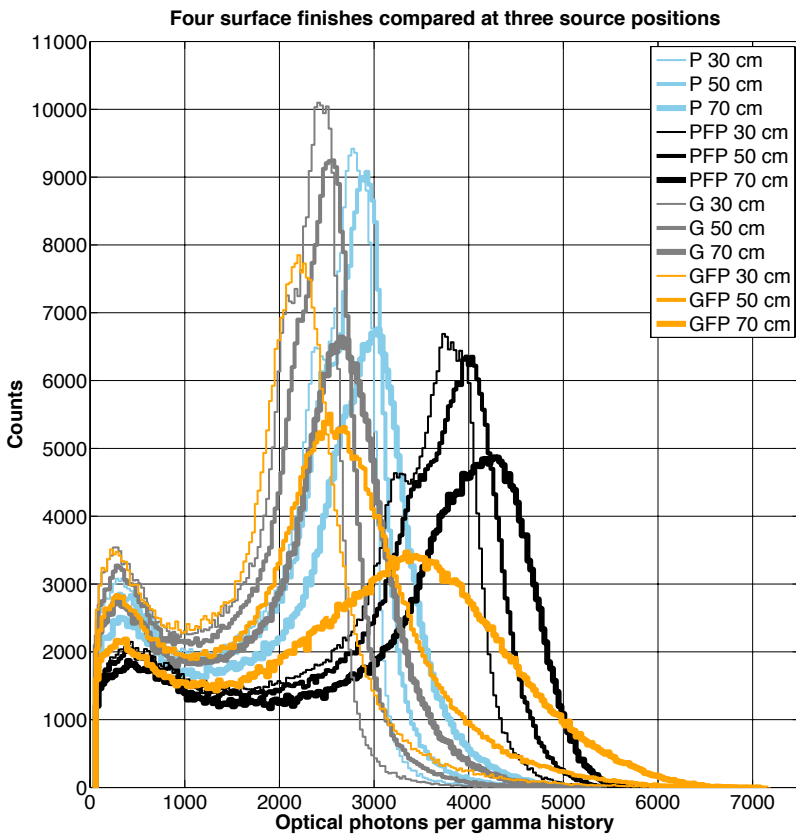

Figure 15. The optical spectrum scored at three different source positions, 30 cm, 50 cm and 70 cm, for four different surface parameters, P, PFP, G and GFP.

For each surface finish, the optical spectrum shifted as the source was moved away from the photocathode (from 70 cm to 30 cm) and at each source position the optical spectrum shifted with respect to surface finish.

4.2.3 C. The PMT multiplication, and
D. Verification of the GATE model of the WBC system

Figures 16 – 18 show the measured energy spectrum, the optical spectrum and the PMT spectrum for ^{137}Cs, ^{54}Mn and ^{65}Zn, respectively, at the source positions 30 cm, 50 cm and 70 cm. Channel (bin) size is 40 optical photons for the optical spectrum and $4.8 \cdot 10^9$ electrons for the PMT spectrum. The PMT spectrum was calculated for δ = 5.5 (compared to δ = 5 and 6, δ = 5.5 gave the best agreement between the PMT spectrum and the measured energy spectrum). All results were obtained for detector 1 in Figure 9.

The dead times in the measurements were 16 –19 % for ^{137}Cs and 0 % for ^{54}Mn and ^{65}Zn.
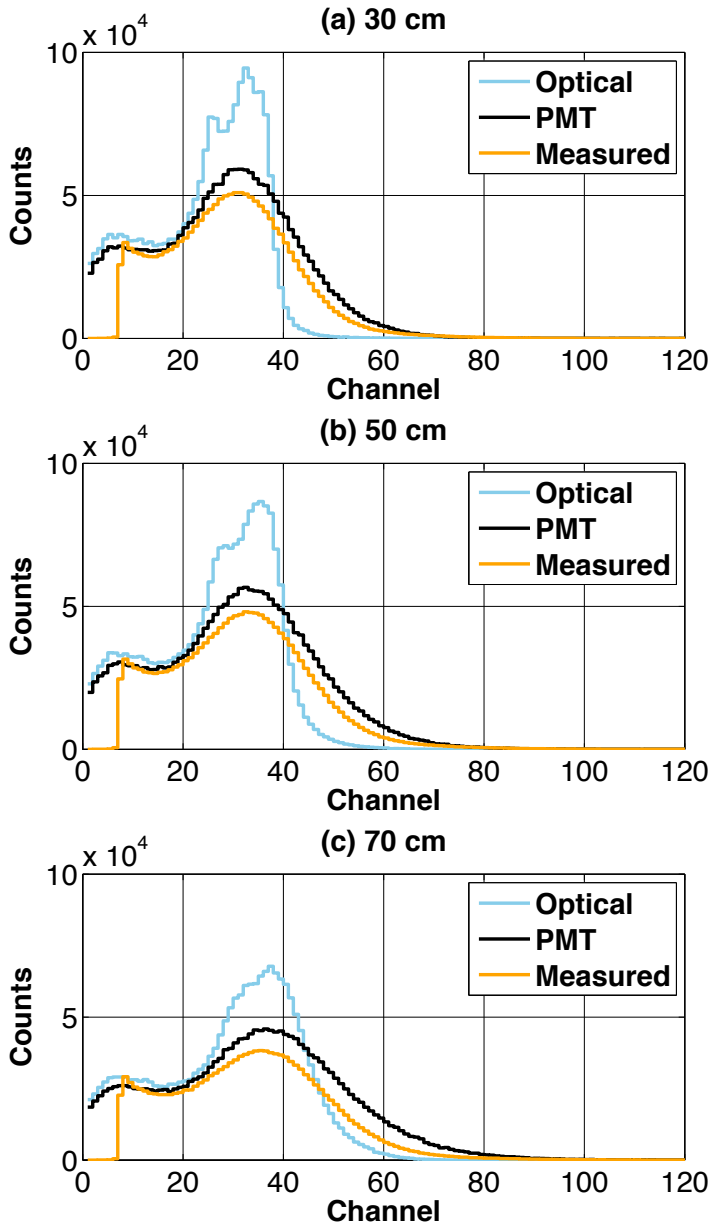
Figure 16(a-c) The measured energy spectrum, the optical spectrum and the PMT spectrum for ^{137}Cs obtained for three source positions.
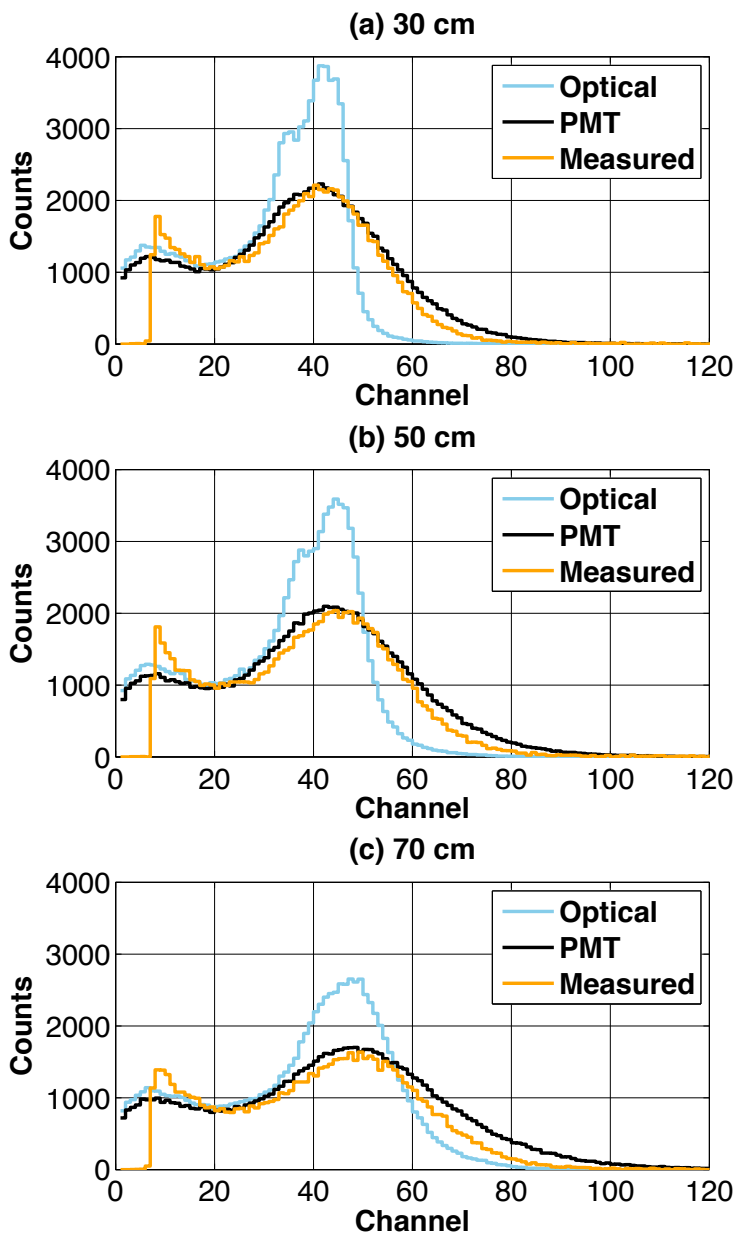
Figure 17(a-c) The measured energy spectrum, the optical spectrum and the PMT spectrum for ^{54}Mn obtained for three source positions.
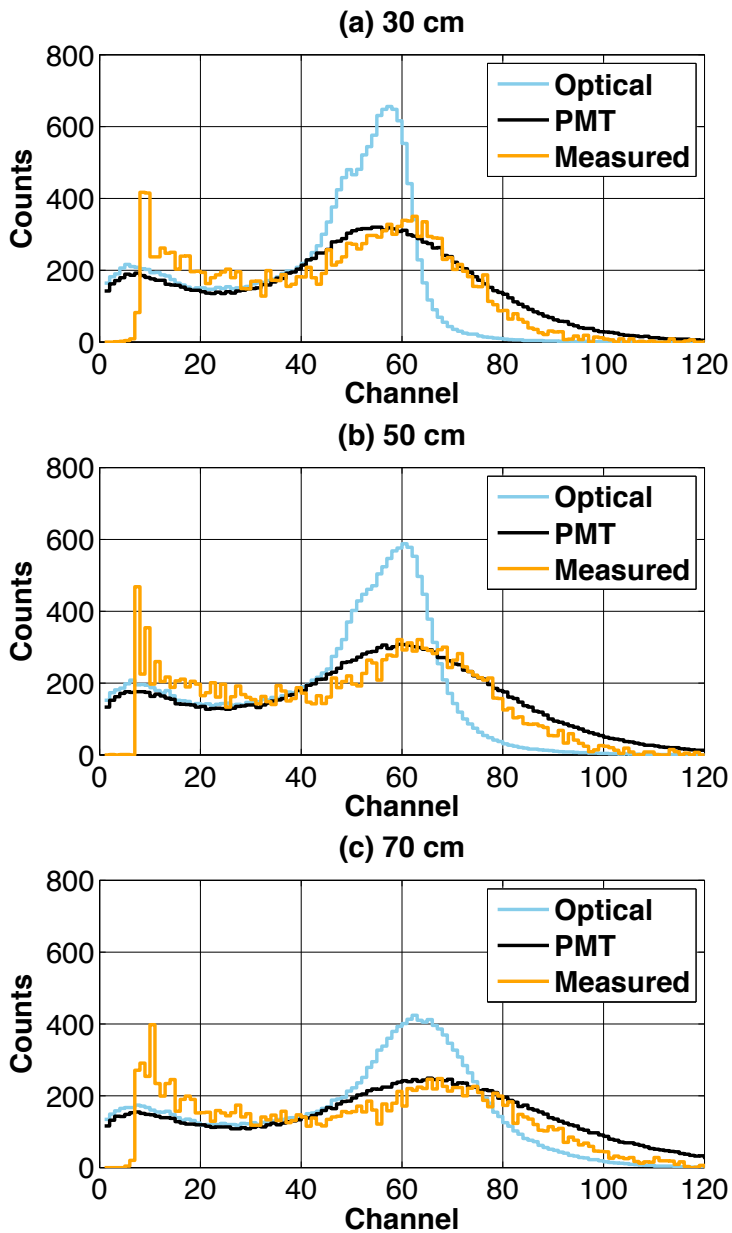
Figure 18(a-c) The measured energy spectrum, the optical spectrum and the PMT spectrum for ^{65}Zn obtained for three source positions.

For each spectrum in Figures 16 – 18, Tables 1 – 3 show the total efficiency, ε, (see section 3.2.1) calculated using the optical spectrum, $\varepsilon_{TotOptical}$, the PMT spectrum, ε_{TotPMT}, and the measured spectrum $\varepsilon_{TotMeasured}$. In all spectra, channels 1 – 9 were excluded in the calculation of the total efficiency [4].

Table 1. The total efficiency for ^{137}Cs at each source position.

Total efficiency \ Source position	$\varepsilon_{TotOptical}$	ε_{TotPMT}	$\varepsilon_{TotMeasured}$
30 cm	0.35	0.36	0.30
50 cm	0.36	0.37	0.31
70 cm	0.35	0.35	0.27

Table 2. The total efficiency for ^{54}Mn at each source position.

Total efficiency \ Source position	$\varepsilon_{TotOptical}$	ε_{TotPMT}	$\varepsilon_{TotMeasured}$
30 cm	0.35	0.36	0.33
50 cm	0.37	0.37	0.34
70 cm	0.35	0.35	0.31

Table 3. The total efficiency for ^{65}Zn at each source position.

Total efficiency \ Source position	$\varepsilon_{TotOptical}$	ε_{TotPMT}	$\varepsilon_{TotMeasured}$
30 cm	0.35	0.36	0.35
50 cm	0.36	0.37	0.35
70 cm	0.35	0.35	0.32

---

[4] The discrimination level was set at channel 8 in the measured energy spectrum. When calculating the total efficiency the discrimination level was set at channel 9 for all spectra.

Figure 16 shows that the PMT spectrum overestimates the number of scored counts compared to the measured spectrum at each source position for ^{137}Cs. Figure 17 and Figure 18 show a good, but not perfect, agreement between the PMT spectrum and measured spectrum at each source position for ^{54}Mn and ^{65}Zn, respectively. Tables 1 – 3 show that the simulations overestimate the total efficiency, this is especially noticeable for ^{137}Cs presented in Table 1.

4.2.4   E. The ICRP Computational Phantom for the Reference Male and Reference Female

Figure 19 and Figure 20 show the PMT spectrum obtained for each detector in the WBC for a ^{137}Cs distribution and a ^{40}K distribution, respectively, in the Reference Male and Reference Female computational phantom. Both figures show that there is only a small difference in detector response between the Reference Male and Reference Female. Notice that the y-axis begins at 10^2 counts; Figure 21 and Figure 22 show the entire y-axis. For ^{137}Cs the total efficiency was 0.62 for the Reference Female and 0.59 for the Reference Male. For ^{40}K the total efficiency was 0.59 for the Reference Female and 0.56 for the Reference Male.

Figure 21 and Figure 22 show the combined PMT spectrum from all four detectors for the Reference Female with heterogeneous distributions of ^{137}Cs and ^{40}K. In Figure 21 the number of source particles for ^{40}K was equal to the number of source particles for ^{137}Cs. In Figure 22 the counts in the PMT spectrum for ^{40}K was scaled to correspond to a fraction of 0.1 source particles relative to ^{137}Cs. Both figures show that it is possible to distinguish two nuclides in a PMT spectrum obtained using a plastic scintillator despite the poor energy resolution.

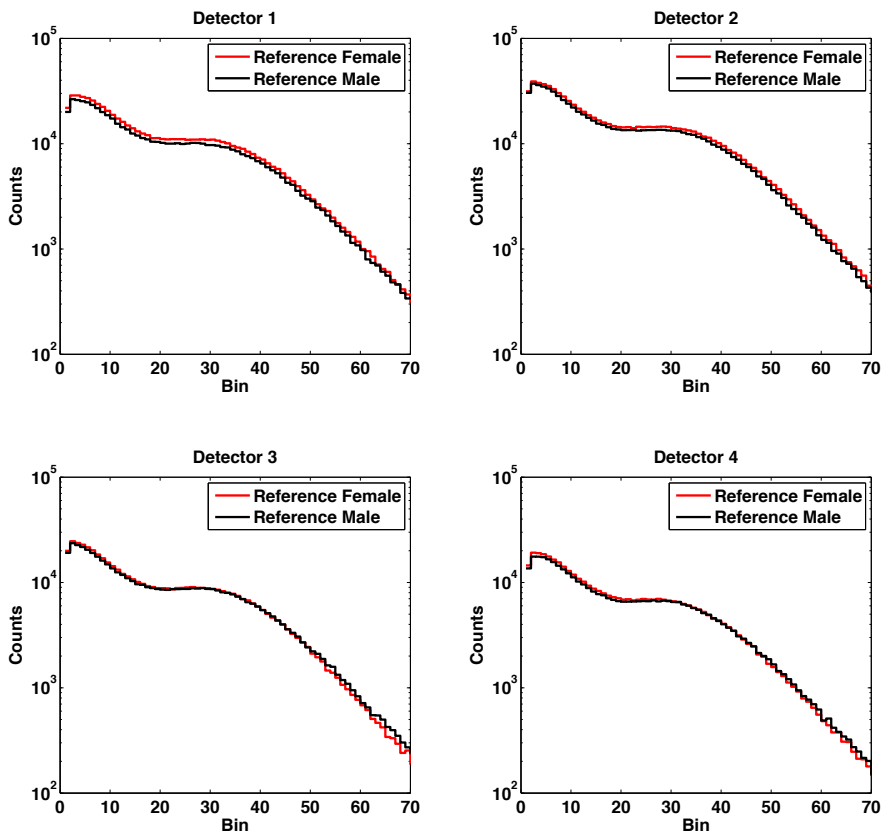The simulation time for one PMT spectrum was about 22 hours on a MacBook Pro 2.3 GHz Intel Core i7.

Figure 19. The PMT spectrum per detector for the Reference Female phantom and Reference Male phantom with a heterogeneous source distribution of ^{137}Cs.
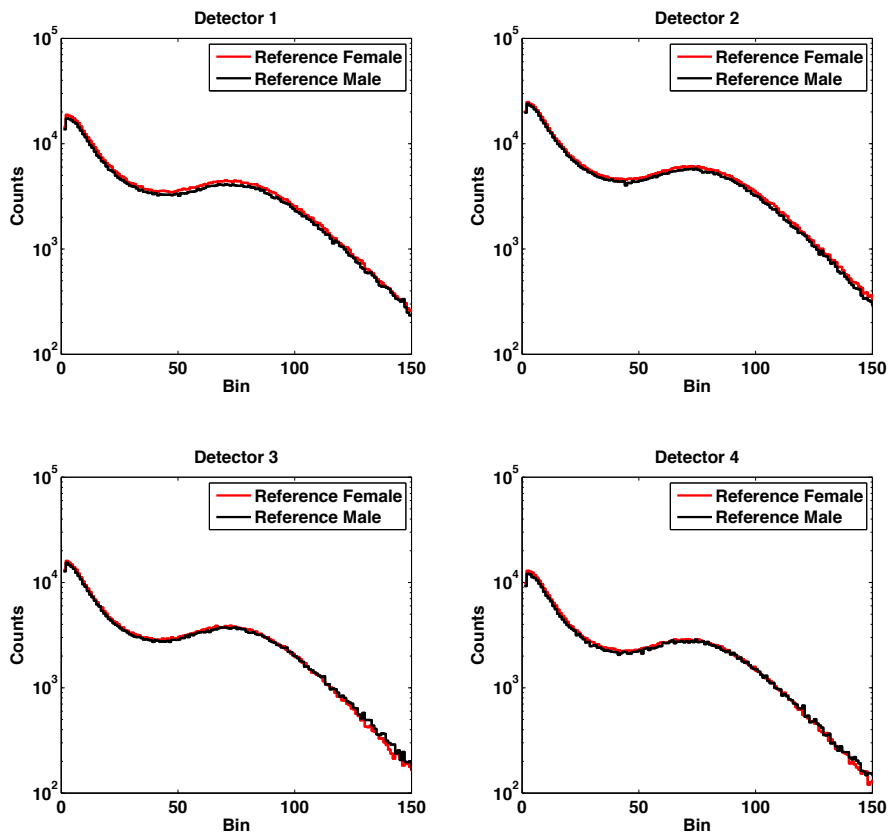
Figure 20. The PMT spectrum per detector for the Reference Female phantom and Reference Male phantom with a heterogeneous source distribution of ^{40}K.

Figure 21. The PMT spectrum (summed from detector 1–4) for the Reference Female phantom with a heterogeneous source distribution. A PMT spectrum was obtained for ^{137}Cs, ^{40}K and ^{137}Cs + ^{40}K, respectively. The number of source particles for ^{40}K was equal to the number of source particles for ^{137}Cs.
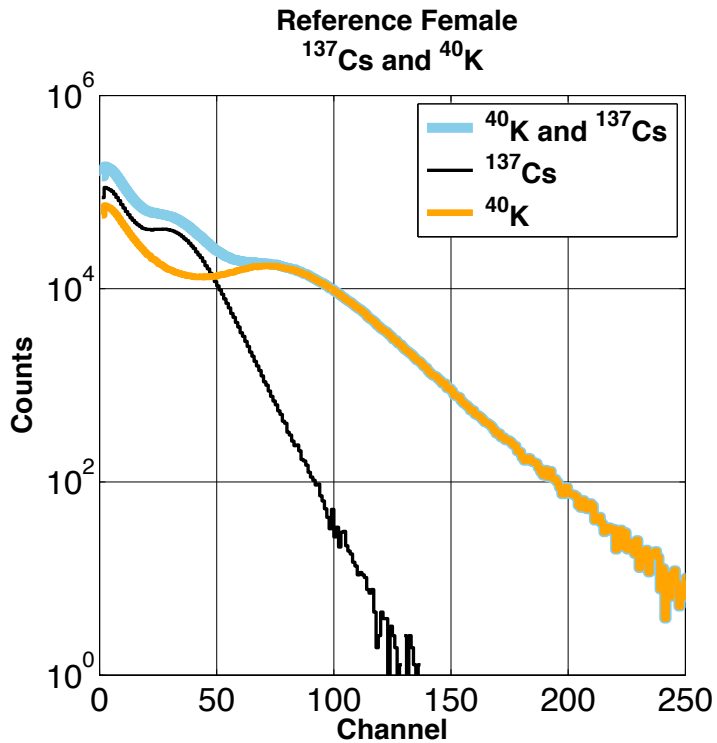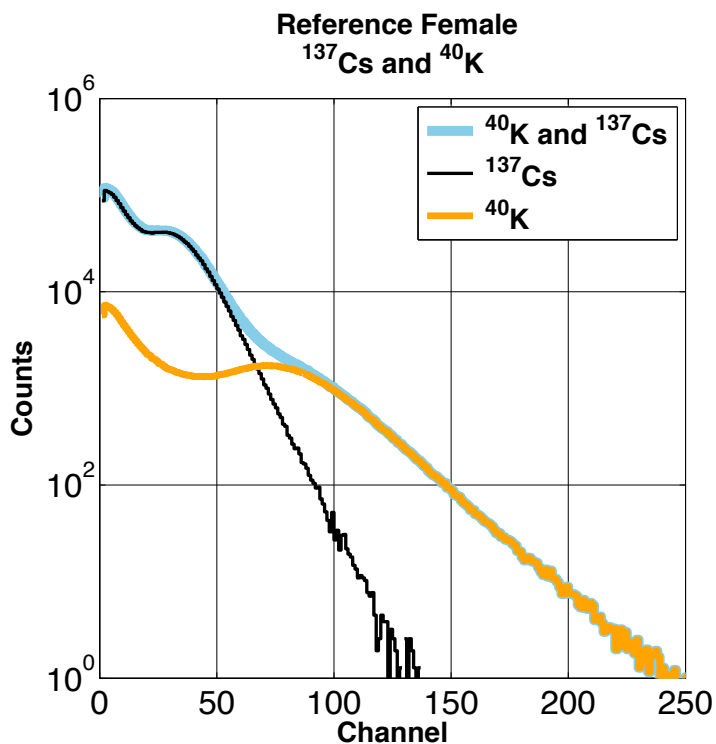
Figure 22. The PMT spectrum (summed from detector 1– 4) for the Reference Female phantom with a heterogeneous source distribution. A PMT spectrum was obtained for ^{137}Cs, ^{40}K and ^{137}Cs + ^{40}K, respectively. The number of counts for ^{40}K was scaled to correspond to a fraction of 0.1 source particles relative to ^{137}Cs.

5 DISCUSSION

5.1   Paper I

To achieve a simulated energy spectrum equivalent to a measured energy spectrum it is not uncommon to use a Gaussian broadening function on a simulated energy deposition spectrum. In Paper I it was argued that such a broadening function would not be sufficient since it would not account for the loss of optical photons. Instead it was suggested using the broadening function first proposed by Breitenberger [16]. The geometrical Monte Carlo model of the WBC needed to be verified so that a broadening function could be implemented, but first after the broadening function had been implemented would it be possible to compare the simulated energy spectrum with measured energy spectrum. As an attempt to solve this catch 22, the total efficiency was studied since it is independent of spectrum resolution. Due to the size of the plastic scintillator there is a source position sensitivity and if there was an agreement between simulated total efficiency and measured total efficiency for a range of source positions it would be a strong indication that the geometrical model was a sufficient description of the WBC.

There is a good agreement between simulated total efficiency and measured total efficiency at all source positions, except for close to the plastic scintillator edges. However, the discrimination applied to the measured energy spectrum could not directly be incorporated in the simulations since the relationship between channel and energy in a measured energy spectrum is unknown. The proposed method to solve this, discriminate the simulated spectrum until the simulated and measured total efficiency matched, is not satisfactory. The simulated results are not compared to measured results; instead simulated results are adapted using the measured results by which they are also compared. Further, a measured energy spectrum shifts with respect to source position. The discriminated channels, 1 – 8, will not correspond to the same energy level at all source positions, this was not accounted for in the discrimination of a simulated energy deposition spectrum.

The results give an indication that the geometrical model is sufficient, but it is not as strong as first expected due to the discrimination in the measured energy spectrum.

5.1.1   Study the impact of a nonlinear light yield

Craun and Smith [54] have published a summary of Birks' constant kB for NE 102 (NE 102 is equivalent to NE 102A, see section 2.1.4) extracted from fits of Birks' formula to 8 sets of experimental data, where 7 were previously published by other authors. The values for kB are in the range 2 – 13.2 mg cm^{-2} MeV^{-1} where 6 values of kB were in the range 9.1 to 13.2 mg cm^{-2} MeV^{-1}. Other reported values for kB are 8.82 and 9.21 mg cm^{-2} MeV^{-1} [55]. The value for kB calculated in this work, kB = 9.6 mg cm^{-2} MeV^{-1}, is in good agreement with previous published values.

No difference between a nonlinear light yield spectrum and linear light yield spectrum was observed. It could be that the nonlinearities are too small to be noticed with the resolution 0.001 MeVee. Moreover, the MCNPX code assumes that energy deposited by a gamma photon is absorbed locally, i.e. photoelectrons or Compton scattered electrons are not transported. If all electrons were to be transported the results might have shown impacts of a nonlinear light yield.

5.2   Paper II – IV

5.2.1   The origin of the full energy peak

The probabilities for photoelectric absorption and Compton scattering are about equal for gamma energies of 20 keV. For gamma energies above 100 keV the probability for photoelectric absorption is less than 1 % [19]. For the plastic scintillator with radius 1 cm, Figure 14a, only 0.0034 % of the particle histories deposited their entire energy through photoelectric absorption. Despite the low contributions from photoelectric absorption there is a full energy peak even for a small plastic scintillator. The hypothesis was that a gamma photon could deposit its entire energy through multiple Compton scatterings. Figure 14 confirms this as the main contribution to the full energy peak comes from particle histories with one or more scored Compton scatterings. The poor energy resolution for the plastic

scintillator, as seen in Figure 1, is clearly not du to the lack of full energy deposition events.

5.2.2 B. Definition of the surfaces in the GATE model

Paper II was a small study where it was investigated if the WBC response could be modeled using GATE. Unlike MCNPX and GEANT4, GATE is not a general-purpose code and has geometrical restraints and limitations the available physics. If GATE could be used then optical transport could be included in the simulations (impossible in MCNPX), without any knowledge about C++ (as for GEANT4). The specifications that needed to be fulfilled was that the geometrical properties of the WBC could be defined in GATE, that the energy deposition and optical photons per particle history could be scored for the plastic scintillator and that the scored data would be in a format suitable for further data processing.

The results from Paper II were very promising. The geometrical model of the WBC could be defined (except for the lightguides, this is addressed in section 5.2.3) and it was possible to simulate the energy deposition in the plastic scintillator and the following optical transport and their detection by a photocathode surface. By enabling the ASCII output option in GATE the energy deposited and detected optical photons per particle history were scored column wise, which made it suitable for further data processing.

It was concluded that the surface parameters, which control the optical physics processes an optical photon undergo at surface boundaries, needed to be investigated further. This was the motivation for Paper III, which was a large study of how the transport of optical photons is modeled in GEANT4.

Figure 15 is a very striking figure and shows the impact on the optical spectrum for one of the most important surface parameters, the surface finish. Figure 15 shows the result from 12 simulations, an optical spectrum was simulated at three source positions, 30 cm, 50 cm and 70 cm, for four surface finishes PFP, GFP, P and G. The four surface finishes were used for defining the plastic scintillator surface facing the air gap, see Figure 10 and Figure 11. Figure 15 shows that the optical spectrum is sensitive to source position, which is also seen in the measured energy spectrum, see Figure 1. The energy deposition spectrum at each source position is the same regardless of surface finish and the difference in the optical spectrum

at each source position, with respect to surface finish, is caused solely by the optical transport.

The surface finish PFP reflects all optical photons at the plastic scintillator – air boundary and the reflective angle is equal to the incident angle. No optical photons leave the plastic scintillator and the shifts in the optical spectrum between source position 30 cm, 50 cm and 70 cm are caused by bulk absorption. As the source is moved away from the photocathode the energy deposition is localized further away from the photocathode and the mean distance traveled in the scintillator before reaching the photocathode for the generated optical photons increases. This leads to an increased loss of optical photons due to bulk absorption, which is shown as a shift in the optical spectrum.

The surface finish GFP also reflects all optical photons at the plastic scintillator – air boundary but here the reflection angle is calculated with respect to a rough surface. This leads to a more erratic path for the optical photons and the distance traveled in the scintillator increases. This explains why the optical spectrum for GFP is shifted relative to the optical spectrum for PFP at each source position.

The surface finish P allows optical photons to be refracted and leaving the scintillator volume or reflected at the plastic scintillator boundary. The reflective angle is equal to the incident angle. Compared to the optical spectrum for PFP at each source position, the optical spectrum for P shifts since more optical photons can be lost through both refraction and bulk absorption.

The surface finish G allows optical photons to be refracted and leaving the scintillator volume or reflected at the plastic scintillator – air boundary. The reflective angle is calculated against a rough surface. This leads to a more erratic path for the optical photons and at each source position the optical spectrum for G shifts relative to the optical spectrum for P.

Figure 15 clearly shows that generation of optical photons and their transport through the scintillator are a major contribution to the poor energy resolution in the measured energy spectrum seen in Figure 1. Figure 15 also shows that the source position sensitivity seen in a measured energy spectrum is cause by optical transport (and verified the conclusions drawn from the small work presented in Figure 2).

Other available surface parameters can alter the surface properties further. For example: a surface parameter controls if an optical photon is

absorbed by a surface instead of reflected or refracted, another surface parameter controls the roughness of a surface, several surface parameters control how the reflection angle for a rough surface should be calculated etc. How each surface parameter controls the optical physics and its impact on the optical spectrum is presented in Paper III. Paper III aimed to be at use for the GEANT4 and GATE community working with optical transport, but since all simulations were done using the GATE model of the WBC the results from Paper III also showed the most suitable surface parameters for the WBC. This is further addressed in section 5.2.3.

5.2.3   C. The PMT multiplication, and
D. Verification of the GATE model of the WBC system

Figures 16 – 18 show that the addition of optical transport and PMT multiplication in the GATE model results in a PMT spectrum quite similar to a measured energy spectrum. Though, it is not a perfect match. In Figure 16 the PMT spectrum for ^{137}Cs overestimates the number of scored counts in nearly all channels compared to the measured energy spectrum. The total efficiencies presented in Tables 1 – 3 also show that the simulated total efficiency is greater than the measured, especially for ^{137}Cs. To explain or understand the differences it is important to understand how the GATE model describes the WBC system (and what is not described).

The differences between the GATE model and the WBC in system II
1. Geometrical properties
Geometrical properties such as patient bed suspension, plastic scintillator suspension inside the detector housing, surrounding walls, bolts in the detector housing etc. are not included in the GATE model, and these kinds of simplifications will have an impact the simulated energy deposition spectrum. Tests were made with and without the twin steel chamber walls and the change in the energy deposition spectrum was barely noticeable. It is assumed that the geometrical simplifications mentioned above will have a minor impact on the final PMT spectrum compared to other simplifications or uncertainties in the GATE model.

   One geometrical simplification and its impact on the optical spectrum that needs to be addressed is the exclusion of the lightguides, which had to be omitted because the couplings between plastic scintillator, lightguide and PMT are unknown as well as the lightguide properties. This means

that a part of the optical transport was excluded and since optical photons are a part of the signal this ought to affect the optical spectrum.

The GATE model describes a WBC where each detector consists of a plastic scintillator and mounted directly at one of the scintillator's short ends is a PMT with a rectangular end window in the same size as the plastic scintillator short end. The GATE model does not account for loss of optical photons at the plastic scintillator – lightguide coupling. Neither does it account for loss of optical photons in the lightguide nor the loss of optical photons at the lightguide – PMT coupling. If the processes leading to a loss of optical photons would be included in the GATE model and the re-simulated optical spectrum would be shown together with the current optical spectrum in Figures 16 – 18, then the re-simulated optical spectrum would be shifted at each source position. That is, if the bin size was 40 optical photons/channel as for the optical spectrum obtained without lightguide. If the bin size was re-calculated with respect to the re-simulated optical spectrum, using the method described in section 3.3.4, then the results might be quite similar to those now presented in Figures 16 – 18; given that all particle histories loose the same fraction of optical photons. The same would apply for the PMT spectrum since the gain factor does not depend on the number of released photoelectrons. The bin size would decrease for both the optical spectrum and the PMT spectrum, the absolute number of detected optical photons and produced electrons would decrease, but the number of scored counts would be the same.

This is an ideal description of how the exclusion of the lightguides will affect the optical spectrum. Most likely have the exclusion of the lightguides resulted in a better spectrum resolution, a variance in the fraction of optical photons lost per particle history will result in a deterioration of the optical spectrum resolution.

2. Surface parameters

The plastic scintillator surface properties are unknown, but with the results from Paper III it was possible to make a well-educated guess of how the plastic scintillator surface should be defined in GATE. The plastic scintillator surface should not have a reflective coating/paint. The shift in the optical spectrum with respect to source position should be small, see Figure 1. There are only two choices for describing a surface without any coating: polished and ground. Ground was chosen since it has a slightly

smaller shift in the optical spectrum with respect to source position. The reflectivity was set to 1.0, Paper III had showed that a reflectivity < 1 resulted in an increased shift with respect to source positions. To simulate the physics processes for a ground surface the reflectivity type can be set to specular lobe, backscatter or Lambertian, or a mix of all three. Specular lobe was chosen since this gave the smallest shift in the optical spectrum with respect to source position.

To correctly define of the surfaces needed in optical transport simulations can be quite complicated since the surface properties are not always known or measureable. Janecek and Moses [34] and Roncali and Cherry [40] have proposed a method where the physics processes an optical photon undergoes at a surface is determined using measured data instead of calculating the physics processes for a theoretical model of the surface. Janecek and Moses used an experimental set-up specific for their detector geometry whereas Roncali and Cherry used 3D atomic force microscopy (AFM) in a set-up more adaptable to different detector geometries. The angular distribution of reflection angles for an optical photon with a specific incident angle was measured and stored in a lock-up-table (LUT). The LUT was then implemented in the optical transport simulations and when an optical photon reached a surface the reflection angle was sampled from the LUT for the specific incident angle. Roncali and Cherry [40] also used LUT of measured data to determine if an optical photon was reflected or absorbed by the surface. Both work showed a good agreement to experimental data and the usage of LUT can be, but have not been, incorporated in the standard GATE and Geant4 simulation toolkits.

3. Material parameters

All except two surface parameters (Rayleigh scattering length and resolution scale) could be obtained from the manufacturer of the plastic scintillator (Saint Gobain Crystals, France). The Rayleigh scattering length was found in the literature [38]. The production of scintillation (optical) photons depends on energy deposition. In GEANT4 the number of produced optical photons per energy deposition event is sampled from a Gaussian distribution given by resolution scale × (deposited energy × optical photons/MeV)$^{1/2}$. No value was found for resolution scale and it was set to 1 in the GATE model presented in Paper II – IV. A smaller standard deviation

ought to give a less smeared optical spectrum, which ought to give a less smeared PMT spectrum.

4. The PMT model

The response of the PMT in the GATE model assumes that the multiplicative events in the dynode chain are independent of each other. This might be an oversimplification but giving a correct statistical description of the PMT is quite difficult. For future works there are two choices for modeling the PMT, either the PMT response is modeled theoretically, as in this work, or the PMT response is modeled based on experimental results. In the writing moment the choice has not yet been made.

5. Dead time correction and coincidence summing

The GATE model does not include the detection system dead time and coincidence summing. During the dead time the detector system cannot register events and particles depositing energy in the detector will not be registered, i.e. there is a loss of counts. Compared to the measured total efficiency, the GATE model overestimates the total efficiency for all three nuclides. This is most noticeable for ^{137}Cs, which also have the highest dead time, 16 – 19 %. The MCA prolongs the measurement time to account for dead time losses but at high count rates this correction might not have been sufficient.

In cascade decay two or more particles are emitted within picoseconds. Most detectors are not able to differentiate this as separate events and the sum of the energy deposited by the particles is scored in the measured energy spectrum. For emergency preparedness purposes the GATE model ought to be able to model coincidence summing. For example ^{60}Co can be released after nuclear accidents and ^{60}Co cascade decays.

It is possible to model time-dependent events such as dead time and coincidence in GATE. For future work these features ought to be investigated further. GATE has, so far, been successful in modeling the WBC response, it seems likely that GATE can also be used for modeling dead time losses and coincidence summing in the WBC.

5.2.4 E. The ICRP Computational Phantom for the Reference Male and Reference Female

Other than the ICRP computational phantoms there are numerous voxel phantoms; whole body voxel phantoms of human at various ages, voxel phantoms of only a part of the body, different level of details, mouse voxel phantoms etc. [58]. The ICRP computational phantoms were chosen because they are well documented and it also makes it possible to couple the WBC response to an effective dose[5]. ICRP has defined age dependent physical and biokinetic models for a large range of nuclides to calculate "the dose per unit intake to the public" [43] which are used to calculate the effective dose using the ICRP Reference Male and Reference Female. The effective dose for a nuclide with known activity can be calculated with the software IMBA (Integrated Modules for Bioassay Analysis) [59], which is based on the ICRP models.

Figure 19 and Figure 20 show that the individual detector response in the WBC for a ^{137}Cs source distribution and ^{40}K source distribution, respectively, is similar for the Reference Male and the Reference Female computational phantoms. The total efficiency was slightly higher for the Reference Female for both source distributions, this since it is a smaller phantom and less source particles ought to be absorbed in the phantom before reaching the detectors. Both figures show that the response from each detector is slightly different due to the heterogeneous source distributions and anthropomorphic phantoms.

Figures 19 –22 clearly show the advantage of a Monte Carlo calibration of a WBC. By including a computational phantom in the GATE model the response for a heterogeneous source distribution in a heterogeneous and anthropomorphic phantom can be simulated. To simulate one PMT spectrum takes about 22 hours but four simulations, one for each detector in the WBC, can run parallel. Hence the WBC can be calibrated for a wide range of nuclides in numerous distributions within a short notice.

---

[5] The effective dose is used to estimate the risk for a population after exposure of ionizing radiation. It should not be used to estimate the dose to an individual.

6 CONCLUSIONS AND FUTURE AIMS

This thesis has showed the importance of correctly modeling the radiative processes in a plastic (organic) scintillator when making a Monte Carlo simulation of its response to ionizing particles. The Monte Carlo model in this work included the energy deposition by a gamma photon in the scintillator, the following generation and transport of optical photons, the detection of optical photons at a photocathode and PMT multiplication. Due to the detailed modeling of the radiative processes in a scintillator the Monte Carlo simulated PMT spectrum showed a good agreement to a measured energy spectrum.

The Monte Carlo model was defined in the Monte Carlo code GATE. A special attention has been given to the surface parameters in GEANT4/GATE that control the physics processes an optical photon undergoes at a volume boundary. To improve the agreement between simulated energy spectrum and measured energy spectrum the same attention ought to be given to the material parameters that control the scintillation and the transport of optical photons through a material. Dead time losses and coincidence summing are not included in the GATE model and the possibility to model this using GATE ought to be investigated further.

The aim of the thesis was to develop a Monte Carlo calibration of a WBC consisting of four large plastic scintillators and this was made possible by including the ICRP computational phantoms in the GATE model. It was shown that the WBC response for a heterogeneous source distribution in an anthropomorphic phantom could be Monte Carlo simulated.

In Sweden there are currently 12 laboratories capable of whole body measurements located at authorities, universities and nuclear facilities [60]. The results and knowledge gained from this thesis can be used for developing Monte Carlo calibrations of the WBC systems at these facilities.

7 ACKNOWLEDGEMENTS

^_^

8 REFERENCES

[1] Sköldborn H, Arvidsson B and M. Andersson 1972 A New whole body monitoring Laboratory *Acta Radiol.* **12** 233–241

[2] Alpsten M, Arvidsson B and Larsson L 1988 Measurements of K-40 in a whole body counter using coincidence technique for correction for Cs-134 contribution, 5th Nordic radioecology Seminar, Rättvik, Sweden

[3] Alpsten M, Ekenved G and Andersson M 1976 A profile scanning method of studying the release properties of different types of tablets in man *Acta Pharm. Suec.* **13** 107-122

[4] Brummer R J, Lonn L, Bengtsson B A, Kvist H, Bosaeus I and Sjostrom L 1996 Comparison of different body composition models in acromegaly *Growth Regulat.* **6** 191-200

[5] Davidsson L, Cederblad Å, Lönnerdal B and Sandström B 1989 Manganese retention in man: a method for estimating manganese absorption in man *Am. J. Clin. Nutr.* **1** 170-179

[6] Ekenved G, Arvidsson B and Sölvell L 1976 Influence of food on the absorption from different types of iron tablets *Scand. J. Haematol* **28** 79-88

[7] Fredlund K, Isaksson M, Rossander-Hulthén L, Almgren A and Sandberg A S 2006 Absorption of zinc and retention of calcium: dose-dependent inhibition by phytate *J. Trace. Elem. Med. Bio.* **20** 49-57

[8] Isaksson M, Alpsten M, Cederblad Å, Larsson L and Pettersson N 2000 In vivo Identification and Localisation of Radioactive Contamination in the Human Body *Radiat. Prot. Dosim.* **89** 317-319

[9] Isaksson M, Bosaeus I, Surac Y and Alpsten M 2003 Determination of potassium in the skeletal muscles by whole-body counting *Acta Dieabetol.* **40** 68-72

[10] Isaksson M, Fredlund K, Sandberg A S, Almgren A and Rossander-Hulthen L 2000 Determination of the retention of 47Ca by whole-body counting *Appl. Radiat. Isotopes* **52** 1441-1450

[11] Johansson A C, Attman P O and Haraldsson B 1997 Creatinine generation rate and lean body mass: a critical analysis in peritoneal dialysis patients *Kidney Int.* **51** 855-859

[12] Johansson A C, Samuelsson O, Haraldsson B, Bosaeus I and Attman P O 1998 Body composition in patients treated with peritoneal dialysis *Nephrol. Dial. Transpl.* **13** 1511-1517

[13]   Ojerskog B, Andersson H, Bosaeus I, Brevinge H and Nilsson L O 1998 Total body water and total body potassium in ileostomy patients before and after conversion to the continent ileostomy *Gut* **29** 1198-1201

[14]   Rudin A, Bosaeus I and Hessov I 1990 Total body potassium, skeletal muscle potassium and magnesium in patients with Bartter's syndrome *Scand. J. Clin. Lab. Inv.* **50** 273-277

[15]   Tengvall M, Ellegard L, Bosaeus N, Isaksson M, Johannsson G and Bosaeus I 2010 Bioelectrical impedance spectroscopy in growth hormone-deficient adults *Physiol. Meas.* **31** 59-75

[16]   Breitenberger E 1955 Scintillation spectrometer statistics *Progr. Nuclear Phys.* **4** 56-95

[17]   Nilsson J and Isaksson M 2011 A Comparison between Monte Carlo calculated and measured total efficiencies and energy resolution for large plastic scintillators used in whole-body counting *Radiat. Prot. Dosim.* **144** 555-559

[18]   Pelowitz D B 2008 MCNPX USER'S MANUAL Version 2.6.0. *LA-CP-07-1473* Los Alamos National Laboratory New Mexico USA

[19]   Siciliano E R, Ely J H, Kouzes R T, Schweppe J E, Strachan D M and Yokuda S T 2008 Energy calibration of gamma spectra in plastic scintillators using Compton kinematics *Nucl. Instrum. Meth.* A **594** 232-243

[20]   Takoudis G, Xanthos S, Clouvas A, Antonopoulos-Domis M, Potiriadis C and Silva J 2009 Spatial and spectral gamma-ray response of plastic scintillators used in portal radiation detectors; comparison of measurements and simulations *Nucl. Instrum. Meth. A* **599** 74-81

[21]   Gardner R P and Sood A 2004 A Monte Carlo simulation approach for generating NaI detector response functions (DRFs) that accounts for non-linearity and variable flat continua *Nucl. Instrum. Meth. B* **213** 87-99

[22]   Atanackovic J, Kramer G H and Hogue M 2013 Monte Carlo model of HPGe detectors used in routine lung counting *Appl. Radiat. Isotopes* **79** 94-102

[23]   Knoll G F 2010 *Radiation detection and measurement*, 4[th]ed. John Wiley

[24]   Nilsson J and Isaksson M 2012 Whole body counting with large plastic scintillators as a tool in emergency preparedness – determination of total efficiency and energy resolution *Proceddings Third european IRPA congress Helsinki Finland* 2023-2029

[25] Nilsson J and Isaksson M 2013 The design of a low activity laboratory housing a whole body counter consisting of large plastic scintillators and the work towards a flexible Monte Carlo calibration *Accepted for publication in Progress in Nuclear Science and Technology*

[26] GATE Users Guide V6.2 *www.opengatecollaboration.org* (obtained 2014-01-11)

[27] Jan S, Santin G, Strul D, Staelens S, Assie K, Autret D, Avner S, Barbier R, Bardies M, Bloomfield P M, Brasse D et al. 2004 GATE: a simulation toolkit for PET and SPECT *Phys. Med. Biol.* **49** 4543-4561

[28] Jan S, Benoit D, Becheva E, Carlier T, Cassol F, Descourt P, Frisson T, Grevillot L, Guigues L, Maigne L et al. 2011 GATE V6: a major enhancement of the GATE simulation platform enabling modelling of CT and radiotherapy *Phys. Med. Biol.* **56** 881-901

[29] Geant4 Collaboration Geant4 User's Guide for ApplicationDevelopers *geant4.web.cern.ch* (last updated 6 December 2013)

[30] The MathWorks, MATLAB and Statistics Toolbox Release 2012a, Natick, Massachusetts, United States.

[31] Bea J, Gadea A, Garciaraffi L M, Rico J, Rubio B and Tain J L 1994 Simulation of Light Collection in Scintillators with Rough Surfaces *Nucl. Instrum. Meth. A* **350** 184-191

[32] Hirano Y, Zeniya T and Iida H 2012 Monte Carlo simulation of scintillation photons for the design of a high-resolution SPECT detector dedicated to human brain *Ann. Nucl. Med.* **26** 214- 221

[33] Janecek M and Moses W W 2008 Optical Reflectance Measurements for Commonly Used Reflectors *IEEE Trans. Nucl. Sci.* **55** 2432-2437

[34] Janecek M and Moses W W 2010 Simulating scintillator light collection using measured optical reflectance *IEEE Trans. Nucl. Sci.* **57** 964–970

[35] Nayar S K, Ikeuchi K and Kanade T Surface reflection: physical and geometrical perspectives 1991 *IEEE T. Pattern Anal.* **13** 611-633

[36] Nozka L, Pech M, Hiklova H, Mandat D, Hrabovsky M, Schovanek P and Palatka M 2011 BRDF profile of Tyvek and its implementation in the Geant4 simulation toolkit, *Opt. express* **19** 4199-4209

[37] van der Laan D J, Schaart D R, Maas M C, Beekman F J, Bruyndonckx P and van Eijk C W E 2010 Optical simulation of monolithic scintillator detectors using GATE/GEANT4 *Phys. Med. Biol.* **55** 1659-1675

[38] Riggi S, La Rocca R, Leonora E, Lo Presti D, Pappalardo G S, Riggi F and Russo G V 2010 GEANT4 simulation of plastic sontillator strips with embedded optical fibers for a prototype of tomographic system *Nucl. Instrum. Meth. A*, **624** 583-590

[39] Riggi S, La Rocca P and Riggi F 2011 Introducing third-year undergraduates to GEANT4 simulations of light transport and collection in scintillation materials *Eur. J. Phys.* **32** 329-341

[40] Roncali E and Cherry S R 2013 Simulation of light transport in scintillators based on 3D characterization of crystal surfaces, *Phys. Med. Biol.* **58** 2185-2198

[41] Levin A and Moisan C 1996 A more physical approach to model the surface treatment of scintillation counters and its implementation into DETECT *IEEE Nucl. Sci. Conf. R.* **2** 702– 706

[42] Nilsson J and Isaksson M 2014 A Monte Carlo calibration of a whole body counter using the ICRP computational phantoms *Submitted to Radiation Protection Dosimetry*

[43] ICRP1990 Age-dependent doses to members of the public from intake of radionuclides - Part 1 *Ann. ICRP* **20** ICRP Publication 56

[44] Birks J B 1964 *The theory and practice of scintillation counting* Pergamon Press

[45] Clark D 1974 The intrinsic scintillation efficiency of plastic scintillators for 60Co gamma excitation *Nucl. Instrum. Meth.* **117** 295–303

[46] Saint-Gobain Ceramics & Plastics Inc. 2005 *BC-400, BC-404, BC-408, BC-412, BC-416 Premium Plastic Scintillators*

[47] Madey R and Waterman F M 1974 A time-of-flight spectrometer for neutrons from about 150 MeV to 1 GeV *Nucl. Instrum. Meth.* **114** 483- 487

[48] Pleil M W 1987 Time resolved fluorescence spectroscopy with a fast analog technique: applications to microscopic specimens *Texas Tech University*

[49] Simonetti J J 1987 High Temperature Plastic Scintillator *US Patent 4713198*

[50] ICRP2009 Adult Reference Computational Phantoms *Ann. ICRP* **39** ICRP Publication 110

[51] ICRP2002 Basic anatomical and physiological data for use in radiological protection: reference values *Ann. ICRP* **32** ICRP Publication 89

[52] National Institute of Standards and Technology U.S. Department of Commerce *ESTAR-Stopping Power and Range Tables for Electrons* http://physics.nist.gov/ (last updated 2005)

[53] Mukhopadhyay S 2004 Plastic gamma sensors: an application in detection of radioisotopes *Proc. SPIE* **5198** 62-72

[54] Craun R and Smith R 1970 Analysis of response data for several organic scintillators. Nucl. Instrum. Meth. **80** 239–244

[55] Hirschberg M, Beckmann R, Brandenburg U, Bruckmann H and Wick K 1992 Precise measurement of Birks kB parameter in plastic scintillators *IEEE T. Nucl.Sci.* **39** 511-514

[56] Motulsky H 2010 *Intuitive Biostatistics 2nd ed.* Oxford University Press

[57] EMI Electronics Ltd Valve Division *EMI photomultiplier tubes*

[58] Xu X G and Eckerman K F 2010 *Handbook of anatomical models for radiation dosimetry* CRC Press/Taylor & Francis Group

[59] Birchall A, Jarvis N S, Peace M S, Riddell A E and Battersby W B 1998 The IMBA suite: Integrated modules for bioassay analysis, Radiat. Prot. Dosim. **79** 107-110

[60] Norrlid L R, Halldórsson Ó, Holm S, Huikari J, Isaksson M, Lind B and Roed H 2011 In-vivo whole body measurement of internal radioactivity in the nordic countries *NKS* **238** Nordisk kernesikkerhedsforskning

9 REFERENCES TO FIGURES

(a)   Nilsson J and Isakssson M 2012 Whole body counting with large plastic scintillators as a tool in emergency preparedness – determination of total efficiency and energy resolution *Third european IRPA congress Helsinki Finland* 2023-2029

(b)   *Wikipedia Commons* 2006-06-03
      http://commons.wikimedia.org/wiki/File:S-p-Orbitals.svg

(c)   Left figure: *Wikipedia Commons* 2009-04-27
      http://commons.wikimedia.org/wiki/File:Methane-CRC-MW-3D-balls.png
      Right figure: *Wikipedia Commons* 2006-06-30
      http://commons.wikimedia.org/wiki/File:Sp3-Orbital.svg

(d)   *Wikipedia Commons* 2006-06-30
      http://commons.wikimedia.org/wiki/File:Sp2-Orbital.svg

(e)   *Wikipedia Commons* 2009-08-11
      http://commons.wikimedia.org/wiki/File:Benzene_Representations.svg

(f)   *Wikipedia Commons* 2009-04-27
      http://commons.wikimedia.org/wiki/File:Acetylene-CRC-IR-3D-balls.png

(g)   Birks J B 1964 *The theory and practice of scintillation counting*. Pergamon Press